JGR Oceans

Key Points:

- A new extratropical cyclone tracker is applied to 42 years of global reanalysis to investigate climatology and seasonality of storms
- Ocean basin composite analyses of satellite-derived significant wave height observations show wave dependence on cyclones characteristics
- The North Atlantic Oscillation climate modes show strong influence on cyclone activity and induced wave climate in the North Atlantic

Author Contributions:

Conceptualization: John Lodise, Sophia Merrifield, Clarence Collins, Peter Rogowski, James Behrens, Eric Terrill
Data curation: John Lodise, Sophia Merrifield, Clarence Collins
Formal analysis: John Lodise
Funding acquisition: Sophia Merrifield, Eric Terrill
Investigation: John Lodise, Sophia Merrifield, Clarence Collins, Peter Rogowski
Methodology: John Lodise, Sophia Merrifield, Clarence Collins
Project Administration: Sophia Merrifield, James Behrens, Eric Terrill
Resources: Sophia Merrifield, James Behrens, Eric Terrill

Global Climatology of Extratropical Cyclones From a New Tracking Approach and Associated Wave Heights From Satellite Radar Altimeter

John Lodise[1,2] ![ORCID], Sophia Merrifield[1] ![ORCID], Clarence Collins[3] ![ORCID], Peter Rogowski[1] ![ORCID], James Behrens[2], and Eric Terrill[1]

[1]Coastal Observing R&D Center, Marine Physical Laboratory, Scripps Institution of Oceanography, La Jolla, CA, USA, [2]Coastal Data Information Program, Scripps Institution of Oceanography, La Jolla, CA, USA, [3]Coastal and Hydraulics Laboratory, U.S. Army Engineering Research and Development Center, Duck, NC, USA

Abstract Extratropical cyclones (ECs) produce comparable wave heights and hazardous sea states to those under hurricanes. With strong wind speeds and considerably larger diameters, the impact of ECs on the global wave climate is substantial. Because ECs occur more frequently, move more quickly, and exist in a large variety of sizes and shapes, these storms are not as well documented. Here, we present findings from a global EC tracking algorithm aimed at creating an EC database of wave producing storms. We focus on the major ocean basins of extratropical cyclone activity: The North Atlantic, North Pacific, and Southern Oceans. Our tracking algorithm uses mean sea level pressure fields from the European Centre for Medium-Range Weather Forecasts (ECMWF) high resolution, advanced data assimilating, ERA5 reanalysis over the years 1979–2020. The 42 year-long data set of thousands of cyclone tracks allows seasonal patterns and longer-term trends of EC activity to be analyzed in these ocean regions. In addition, we employ 36 years of satellite radar altimeter-derived significant wave height (H_s) data from 14 inter-calibrated satellite missions to study the wave climate induced by the identified ECs in each basin. The resulting wave climatology compares well with previous results in the mid to high latitudes. We then analyze average wave heights under different EC characteristics, including cyclone translational speed and maximum winds, which have strong effects on wave height variability. Finally, a brief analysis of EC and wave climate under positive and negative phases of the North Atlantic Oscillation is presented.

Plain Language Summary Large storms which occur outside of the tropics, known as extratropical cyclones (ECs), create very large waves that can surpass that of tropical cyclones. These extreme sea states are responsible for coastal hazards including erosion and surge induced flooding. While tropical cyclones, or hurricanes, are well documented by devoted agencies, ECs are more difficult to track given their high occurrence, fast movement, and inconsistency of size and shape. Here we present the results from a tracking algorithm, applied over a 42 year period, aimed at documenting the many ECs which occur over the global oceans with specific focus placed on wave development within these storms. We use satellite measurements of wave heights within the tracked ECs to investigate wave growth and overall wave climate within these storms. In addition to studying the seasonality of ECs and associated wave activity, we show the regional influence of longer time-scale climate variability on the same.

1. Introduction

Extratropical cyclones (ECs) are responsible for some of the most hazardous sea states recorded (Hanafin et al., 2012; Holliday et al., 2006). The associated marine conditions often rival that of hurricanes, producing wave heights on the order of 10 m and strong winds that cause surge, erosion, and flooding. Their high frequency of occurrence and large ocean fetch significantly contributes to marine and coastal hazards. An accurate climatology of these storms and their associated wave climates over both seasonal and longer time periods aids in the preparedness for the related marine hazards and long term effects on coastal infrastructure.

The tropical oceans, spanning 23.5°S–23.5°N, are typically home to the formation of tropical cyclones. Over subtropical regions, roughly defined as 23.5°N(S)–35°N(S), cyclones form that can have mixed extratropical and tropical characteristics, and the regions poleward of 35° latitude are overwhelmingly dominated by ECs. The boundaries of these regions of course shift with changes in the latitudinal oceanic and atmospheric temperature

Supervision: Sophia Merrifield, Eric Terrill

Validation: John Lodise

Visualization: John Lodise

Writing – original draft: John Lodise

Writing – review & editing: John Lodise, Sophia Merrifield, Clarence Collins, Peter Rogowski, James Behrens, Eric Terrill

and moisture gradients as the seasons change in either hemisphere. While tropical cyclones are typically well documented, being easily tracked due their relativity slow translational speeds, distinctive physical structure, and infrequent occurrence, ECs are much less so. Unlike their tropical counterpart, ECs exist in a larger variety of shapes and sizes, lacking the symmetry of tropical cyclones and ranging from 100 to over 1,000 km in diameter. ECs also travel at much faster speeds, being influenced by the synoptic scale trade winds and the jet stream in the mid-latitudes (Neu et al., 2013).

Varying wind-wave orientation within different regions of tropical cyclones has been shown to have large effects on the wave growth and hindcast skill in different cyclone sectors, defined relative to cyclone center and direction of motion (Black et al., 2007; Donelan et al., 1997; Holthuijsen et al., 2012; Wright et al., 2001). Collins et al. (2021) exploited existing databases of well documented tropical cyclones and satellite radar altimeter measurements of significant wave heights (H_s) to perform composite analyses of wave fields over many years (1995–2018) of cyclone events. Collins et al. (2021) highlighted the tendency of hindcasts to underestimate waves in the right sector, where wind direction and storm direction align, resulting in the largest wave growth. Expanding the work of Collins et al. (2021), a goal of the present study is to develop an EC database, akin to that of tropical cyclones, on a global scale in order to facilitate future investigations of wave processes in a similar cyclone-centered reference frame.

While ECs vary significantly in structure compared to tropical cyclones, typically containing a cold front and warm front, the different cyclone regions produce similar instances of varying directional wave development (Hewson & Neu, 2015; Ponce de León & Bettencourt, 2021). Ponce de León and Bettencourt (2021) offers a schematic showing typical EC structure. Similar to that of tropical cyclones, extreme wave heights have been found to occur in the region of ECs where wind and wave directions align, generally in the sector to the right of the cyclone center, relative to cyclone motion (Ponce de León & Guedes Soares, 2014). ECs studied in the North Pacific by Kita et al. (2018) revealed these cyclone regions to produce distinct directional and frequency spectra, while also showing the rear left region of the cyclone to be comprised of swell and wind sea propagating in different directions. In addition, the region of strongest wave growth has been observed to vary during different development stages of ECs (Ponce de León & Bettencourt, 2021).

The global tracking of ECs, especially on timescales covering several decades, cannot be practically achieved by manual methods commonly used to track and report on individual tropical cyclones. Thus, automated tracking schemes must be implemented to catalog the large number of ECs, $O(1000)$, that occur globally on a yearly basis. Due to varying definitions of what constitutes a cyclone, the majority of previous methods have either utilized fields of mean sea level pressure (MSLP) or vorticity, at varying levels in the lower troposphere, from well-known reanalysis products including those from the European Centre for Medium-Range Weather Forecasts (ECMWF) and National Centers for Environmental Prediction (NCEP) (Gramcianinov et al., 2020; Hodges et al., 2003; Neu et al., 2013; Rudeva & Gulev, 2007; Sinclair, 1994; Ulbrich et al., 2009). While relative vorticity is more directly related to the wind field and is more focused on the higher frequency, MSLP is linked directly to the mass field and better captures lower frequency phenomena (Hodges et al., 2003; Neu et al., 2013).

Ponce de León and Bettencourt (2021) used an EC database (M. Serreze, 2009), developed by M. C. Serreze et al. (1997), which used 6 hr, 250 km resolution, sea level pressure fields from the National Center for Environmental Prediction/National Center for Atmospheric Research (NCEP/NCAR) reanalysis, in order to track ECs in the Northern Hemisphere. Compared to the NCEP/NCAR reanalysis, more recent and computationally advanced products, like the ECMWF ERA5 (Hersbach et al., 2020) reanalysis, have considerable improvements in data assimilation and increased resolution (1 hr, 0.25°). Gramcianinov et al. (2020) tracked ECs in the Northern and Southern Atlantic using fields of relative vorticity at 850 hPa from both the ERA5 and the latest Climate Forecast System reanalysis from NCEP, and found both products to be congruous in mean cyclone characteristics, but with a notable 3.7% more ECs found in the ERA5 product due to finer resolution in both time and space.

Our inspection of ECs tracked by Gramcianinov et al. (2020) showed the method has considerable skill in detecting and tracking a large number of cyclones, especially those at higher frequencies and smaller scales, which is an expected result of relative vorticity-based tracking algorithms (Neu et al., 2013). The EC tracker developed here identifies EC centers using fields of MSLP, along with the Laplace of MSLP, using the same ERA5 reanalysis from the ECMWF. While this may limit the detection of smaller scale structures, our tracking method shows improvement in accurately defining cyclone centers compared to that of Gramcianinov et al. (2020). With our focus on large wave producing ECs and the ability to perform cyclone-centered reference frame analyses, as

performed by Collins et al. (2021) and Ponce de León and Bettencourt (2021), we prioritize the accurate detection of cyclone centers over the tracking of smaller scale cyclones. The resulting EC database is focused on the global oceanic regions with the majority of EC activity, namely the North Pacific, North Atlantic and Southern Oceans. For the purpose of this study, the Southern Ocean refers broadly to the entire region south of 25°S. We use this database, which spans the years of 1979–2020, to describe EC climatology, including seasonal to longer term trends of EC abundance and characteristics.

In addition to the EC analysis presented, EC-induced wave climates are investigated in each basin by compositing satellite altimeter observations of H_s. Only observations within ECs are considered. Zieger et al. (2009), Abdalla et al. (2010), Queffeulou (2004), and Ribal and Young (2019) have verified the ability to make high fidelity measurements of H_s through the use of satellite based radar altimeters. Specifically, the use of these large satellite-based data sets of H_s has been proven successful at estimating climatological trends in wave measurements over many cyclones, as well as categorizing extreme wave events (Alves & Young, 2003; Collins et al., 2021; Izaguirre et al., 2011; Ponce de León & Bettencourt, 2021). The collection of this data from satellite, while temporally sparse in repeated observation of the same location, is compiled over the many storms (order of tens of thousands) identified and tracked here, using the 36 year data set by Ribal and Young (2019), which consists of 14 inter-calibrated satellite missions spanning the time period of 1985–2020. Over the analysis period presented here, we procure a dense data set of H_s observations within ECs which allows for global seasonal analysis of EC-induced wave heights. Binned H_s observations are also evaluated on a global scale under varying cyclone intensities and transitional speeds.

Finally we explore the influence of the North Atlantic Oscillation (NAO) on the EC activity and resulting wave climate in the North Atlantic. While it has been shown that EC activity can be regionally affected by many different modes of climate variability (Machado et al., 2021; Mailier et al., 2006; Ulbrich et al., 2009; Xie et al., 2020, and references therein), for the sake of brevity we restrict our analysis to the NAO, which showed the strongest influence during initial investigation. In the North Atlantic we find a basin-wide response of EC activity and characteristics to shifting modes of the NAO, a trend reciprocated in the EC-induced wave climate in the region. The modes of the NAO are defined by the sea level pressure differences between the Subpolar Icelandic Low and Subtropical Azores High. During the positive phase both of these low-frequency sea level pressure tendencies are amplified resulting in a stronger Icelandic Low and higher Azores High, creating a strong dipole in the sea level pressure field. The negative phase of NAO describes the same features having weaker intensities resulting in a much smaller atmospheric pressure difference between the two regions (Marshall et al., 2001). Previous studies have linked the positive phase of the NAO to increases in cyclones count and intensity in the area around the Icelandic Low, especially during the cold months of the year (Pinto et al., 2009; M. C. Serreze et al., 1997). A regional shift of cyclone activity away from the east coast of the US and Canada, toward the Eastern Atlantic, has also been detected during positive NAO (Chartrand & Pausata, 2020; Wang, Wan, & Swail, 2006). Our results show the positive phase of NAO to be associated with faster moving cyclones of stronger intensities along with a basin wide northeast shift in cyclone center density in the North Atlantic.

2. Data and Methods

2.1. ERA5 Reanalysis

The cyclone tracker utilizes fields of MSLP from the ECMWF ERA5 reanalysis (Hersbach et al., 2020). The hourly ERA5 fields are produced on a ~31 km reduced-Gaussian grid using model forecasts from CY41R2 of the ECMWF Integrated Forecast System (IFS) along with 4D-Var data assimilation. The atmospheric model is coupled to the land-surface model, HTESSEL, and the ocean wave model, WAM. Generally, 18 hr forecasts initialized twice daily from the 06:00 and 18:00 UTC hr analyses make up the reanalysis. The data used here spans the years 1979–2020 and is downloaded from the C3S Climate Data Store (CDS), where it has been interpolated to a regular 0.25° latitude/longitude grid at the same hourly resolution.

2.2. Extratropical Cyclone Tracker

The tracking method utilizes both the MSLP fields and the Laplace of the MSLP, defined as $\nabla^2 p = \left(\frac{\partial^2 p}{\partial x^2} + \frac{\partial^2 p}{\partial y^2} \right)$, in order to identify cyclone centers. After calculating the discrete Laplace of the MSLP fields, a 2-D Gaussian

filter is applied in order to smooth out the noisy, second derivative field. The Laplace of the MSLP is proportional to the geostrophic vorticity and being a second derivative, much less dependent on the larger scale background MSLP (Murray & Simmonds, 1991; M. C. Serreze et al., 1997; Wang, Swail, & Zwiers, 2006). The use of the Laplace allows for earlier detection of developing ECs where closed circulation in the wind field can be seen before the MSLP exhibits a closed isobar around the cyclone center, similar to that shown by Sinclair (1994) using relative vorticity fields for the purpose of EC tracking.

Previous MSLP based methods have used neighboring grid point comparisons to find local minima in the 2-dimensional fields to identify low pressure centers (Murray & Simmonds, 1991; M. C. Serreze et al., 1997; Wang, Swail, & Zwiers, 2006). These methods have utilized grids with relatively coarse spatial resolution, the finest being a regular 2.5° latitude/longitude grid with 6 hr temporal resolution. With the ERA5's considerably higher spatial and temporal resolution the previously used point by point comparison becomes computationally expensive over the 42 year period of interest, while also producing noisy fields of many potential low pressure centers. Here, we choose to employ a new method that makes use of existing grayscale image processing tools.

First, the spatially smoothed Laplace fields are converted to grayscale images within the range of 0.02 and 0.038 Pa km^{-2}, such that values less than 0.02 Pa km^{-2} are black (0 on the grayscale) and values greater than 0.038 Pa km^{-2} are white (1 on the grayscale) in the converted image. These thresholds were chosen during initial testing of the algorithm to limit the identification of unrelated smaller scale perturbations in the field, but still detect as many potential EC centers as possible. The majority of values above the upper limit of 0.038 Pa km^{-2} were largely found to exist within ECs. Pinto et al. (2009) found similar values to exist within ECs in the North Atlantic ranging from ~0.02–0.044 Pa km^{-2}. The conversion results in well defined regions of positive Laplace to show up as bright peaks in the grayscale images. Fields of MSLP are also converted to grayscale images in the same fashion using a range from 1,030 hPa to the minimum pressure in the field at each time step, such that bright peaks correspond to low pressure centers. While this decision may limit the detection of weaker, shallow low pressure systems, limiting the range focuses the tracking algorithm on stronger storms with lower pressure centers which are far more relevant for the EC-driven wave environments of interest.

The grayscale images of the MSLP and Laplace fields are then eroded using a gridded disk shaped morphological structuring element with a radius of 0.5° (on same grid as the MSLP fields). Grayscale image erosion is a well known method in the image processing field (Gonzalez et al., 2020). This is performed by centering the structuring element over each pixel in the image and assigning the minimum value of the pixels within the structuring element's neighborhood to the pixel in the center. On the edges where the structuring element falls outside of the original image, the pixels are assigned zero value (black in the grayscale image). The process acts to sharpen regions of positive Laplace and/or low MSLP and remove structures in the field, smaller than ~1°, that are not associated with well developed cyclone activity. Excluding these smaller scale perturbations that would need to be ruled out as potential cyclone centers improves the efficiency and accuracy of linking storm centers in time.

Following the erosion, image reconstruction using each eroded image and the original image is performed on the MSLP and Laplace images, separately, at each time step. This is carried out using the fast hybrid grayscale reconstruction algorithm presented by Vincent (1993). This process performs repeated dilatations of the eroded image until the contour of the eroded image's peaks fit into that of the original image. The result is an image where the low pressure centers have become well defined, flattened peaks, where regional maximums in the Laplace field and minimums in the MSLP fields can be easily identified.

After the reconstruction, the resulting images are turned into binary images, each pixel being defined as part of a cyclone center or background. While this acts to identify a region around the cyclone centers, it does not physically characterize the spatial extent of the full cyclone. At each time step cyclones are identified by regions of low MSLP, large Laplace, or both. The location of the minimum pressure located within each region is defined as the cyclone center at every time step. If there are multiple minimum pressures of the same value found within the region, the center location of the cyclone is chosen at the minimum pressure closest to the centroid of the defined cyclone region. This choice is motivated by the effort to avoid large jumps in center location between time steps ensuring smoother velocity calculations, representative of the overall cyclone motion.

Storm centers are linked together if they reoccur in the next hourly time-step within 160 km of the previous low-pressure center detected. If there are multiple identified centers within 160 km, then the point with the lowest pressure is chosen as the EC center at the second time step. This upper limit on EC velocity, was chosen based
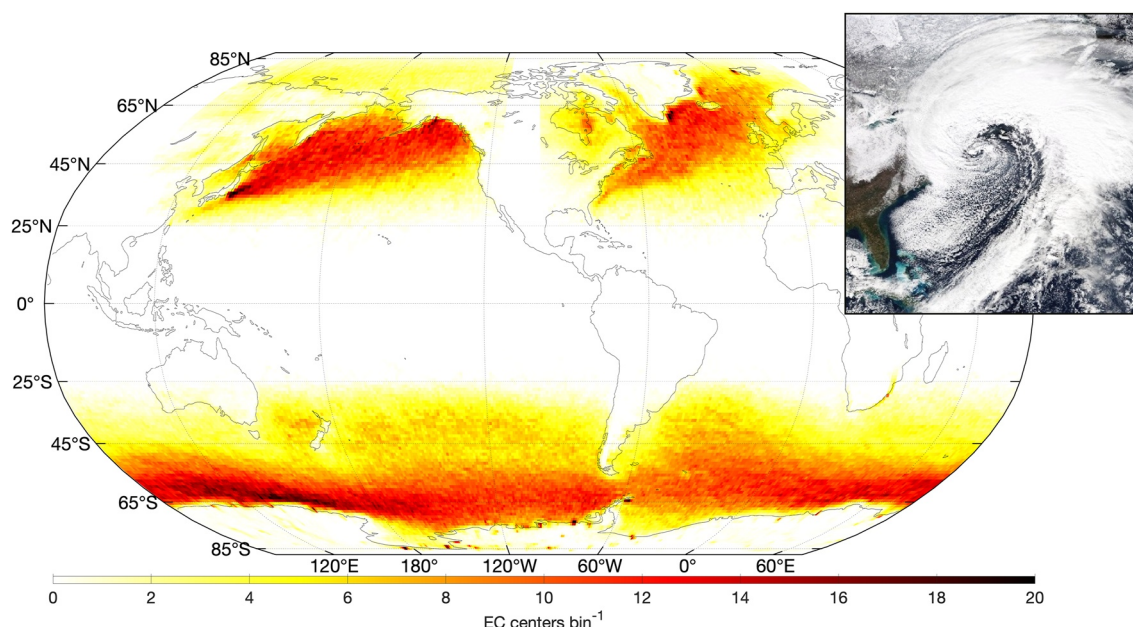
Figure 1. Global annual average EC center density over 42 years, calculated as the number of cyclone centers per year within each 1° × 1° bin shown. Also shown is an inlaid true color image of an Atlantic basin EC taken from the VIIRS/Suomi-NPP satellite on 4 January 2018.

on previously reported velocities of fast moving storms by Bernhardt and DeGaetano (2012), which found winter ECs in the North Atlantic to travel at average velocities up to 40 m s^{-1} (144 km s^{-1}). Neu et al. (2013) states that cyclone velocity is among the most variant characteristics across many different EC tracking methods, partly due to the tendency of certain methods to end storm tracks when rapid cyclone translation occurs. This is often due to necessary restraints on distance traveled when using data sets with coarse time resolution ($\geq$6 hr). The 160 km distance threshold set here allows the fastest moving storms to be tracked during rapid acceleration, while also allowing cyclones with internally shifting pressure centers to be tracked. Gramcianinov et al. (2020) uses a similar distance metric of 2°, emphasizing that the 1 hr temporal resolution of the ERA5 reanalysis decreases the uncertainty when connecting storm centers in time.

The EC tracking algorithm is applied within three different domains that encompass the North Atlantic, North Pacific, and Southern Ocean, separately. In the northern Pacific only ECs that enter into the region bounded by 25°N, 85°N, 120°W, and 120°E are considered. Similarly in the North Atlantic this region is bounded by 25°N, 85°N, 80°W, and 10°E. The Southern Ocean domain has no longitudinal restrictions, but only cyclones which pass between the latitudes of 25°S and 85°S are considered.

EC tracks are smoothed with a third order polynomial Savitzky-Golay finite impulse response filter, which improves the derived storm orientation and translation velocity by lowering the variability of the cyclone center location and allows for off grid velocity calculations. Identified tracks that do not have a minimum duration of 1 day, those that do not move over 1,000 km from the initial detection location, or those that last over 14 days are excluded in order to remove cyclonic features like stationary heat lows and weak very short lived systems.

In order to keep the focus on ECs and not tropical cyclones, the full record of storms that develop between 25°S and 25°N are excluded from the analysis. Cyclones of this nature made up 1.2%, 3.7%, and 2.7% of the total tracked cyclones in the North Atlantic, North Pacific, and Southern Oceans, respectively. While this does allow for some cyclones that form with subtropical characteristics to be included in the data set, cyclones of this type will typically transition to extratropical systems early in their lifetime, before reaching 30–45° North (or South) depending on region and time of the year, as they interact with the baroclinic atmosphere in the mid-latitudes (Hart & Evans, 2001; Jones et al., 2003). S1 shows 6 months of global EC tracks animated over the MSLP fields from the ERA5 reanalysis. Yearly averaged cyclone center density in each basin, along with a visible satellite image of an EC in the North Atlantic from the Visible Infrared Imaging Radiometer Suite (VIIRS) aboard the Suomi National Polar-orbiting Partnership (Suomi-NPP) satellite, can be seen in Figure 1.

2.3. Satellite Altimeter Data and Cyclone-Altimeter Data Pairing

Satellite mounted radar altimeter data has been used previously by Collins et al. (2021) and Ponce de León and Bettencourt (2021) to analyze wave fields under tropical cyclones and ECs, respectively. Satellite altimeter measurements are the only source of H_s observations which can feasibly achieve global coverage, however current application of this platform can only provide information about H_s, defined as the mean of the highest $\frac{1}{3}$ of wave heights. This measurement is derived using the return signal from a nadir directed pulse sent from the satellite based radar. H_s is inferred from the slope of the leading edge of the return signal waveform (Collins et al., 2021). While orbiting satellites can only supply repeat observations at the same location on timescales of 1 week to 1 month, along track resolution is relatively high at 7 km, corresponding to a sampling rate of 1 Hz. This high resolution along track data, collected over a large number of ECs can reveal relationships between cyclone characteristics and H_s measurements (Collins et al., 2021; Ponce de León & Bettencourt, 2021).

To investigate the effects of EC activity and characteristics on the wave climate in the ocean basins of interest, satellite radar altimeter measurements of H_s from the Ribal and Young (2019) database are collected along each cyclone track. The Ribal and Young (2019) database is comprised of H_s and wind data from 14 quality controlled and inter-calibrated satellite altimeter missions spanning the time period from 1985 continuing to present day. We utilize data from all available satellite missions in the data set (GEOSAT, ERS-1, TOPEX, ERS-2, GFO, JASON-1, ENVISAT, JASON-2, CRYOSAT-2, SARAL, JASON-3, HY-2A, SENTINEL-3A, and SENTINEL-3B) from the start time of the data set up until 2020, coinciding with the end of our EC tracking period, for a total of 36 years. As in Collins et al. (2021), we utilize the re-calibrated data ensuring better consistency across time and missions. From the Ribal and Young (2019) quality control nomenclature, we use all data flagged QC-1 ("good data") or QC-2 ("probably good data") following the procedure of Collins et al. (2021), which showed similar results, on average, when using either data type within tropical cyclones. The wind data from altimeter based measurements, being less accurate than that of H_s, were not considered in this study. Cross validations of H_s measurements between satellites resulted in RMSE values less than 0.2 cm for all satellites, where the same procedure for wind measurements resulted in RMSE values an order of magnitude larger.

In order to pair the altimeter data with each EC track, an adapted version of the altWIZ algorithm (Collins & Hesser, 2021), originally developed by Collins et al. (2021) for application with tropical cyclones, is utilized. AltWiz was created as part of the efforts by the U.S. Army Corps of Engineers (USACE) Wave Information Study (WIS) in order to better understand wave development with respect to varying tropical cyclone conditions. Only altimeter data which fall within 500 km and 0.5 hr from each EC center are considered (0.5 hr corresponding to half the time step of the cyclone tracks). The distance threshold of 500 km is chosen based on previous study's of ECs which showed the average EC radius to be approximately 500 km. Ponce de León and Bettencourt (2021) defined a constant EC radius of 500 km as well, based off of a study by Schneidereit et al. (2010) which fit a Gaussian function to the 1,000 hPa geopotential height to estimate the radius and depth of ECs. Schneidereit et al. (2010) found the majority of estimated cyclone radii fell between 300 and 500 km. Composite results of average H_s over many ECs presented by Ponce de León and Bettencourt (2021), showed the highest waves to occur close to, if not on the edge, of the prescribed 500 km radius threshold during the maximum strength of the chosen cyclones. Following these results, we choose a 500 km radius, aware that this threshold is in the upper range of average EC radius found by Schneidereit et al. (2010). Overall 11,710,566 H_s data points are used in the final analysis in the Northern Atlantic, 11,509,979 data points are used in the North Pacific, and 53,343,341 in the Southern Ocean.

3. Results

3.1. Cyclone Tracker Comparison

A comparison of cyclone tracks over 1 month from the algorithm presented here and that of Gramcianinov et al. (2020), referred here after as G20, is provided in Figure 2. While there is general agreement spatially between the plots of cyclone tracks, there are obvious instances where only one method detects a cyclone or coinciding tracks show deviations from one another. This is not unexpected since our method utilizes MSLP fields, and the G20 method uses fields of relative vorticity at 850 hPa. When directly compared, the two types of methods have been shown to produce different total cyclone counts and varying regional densities (Greeves et al., 2007; Hodges et al., 2003; Neu et al., 2013). Figure 2b shows a zoomed instance of a cyclone detected
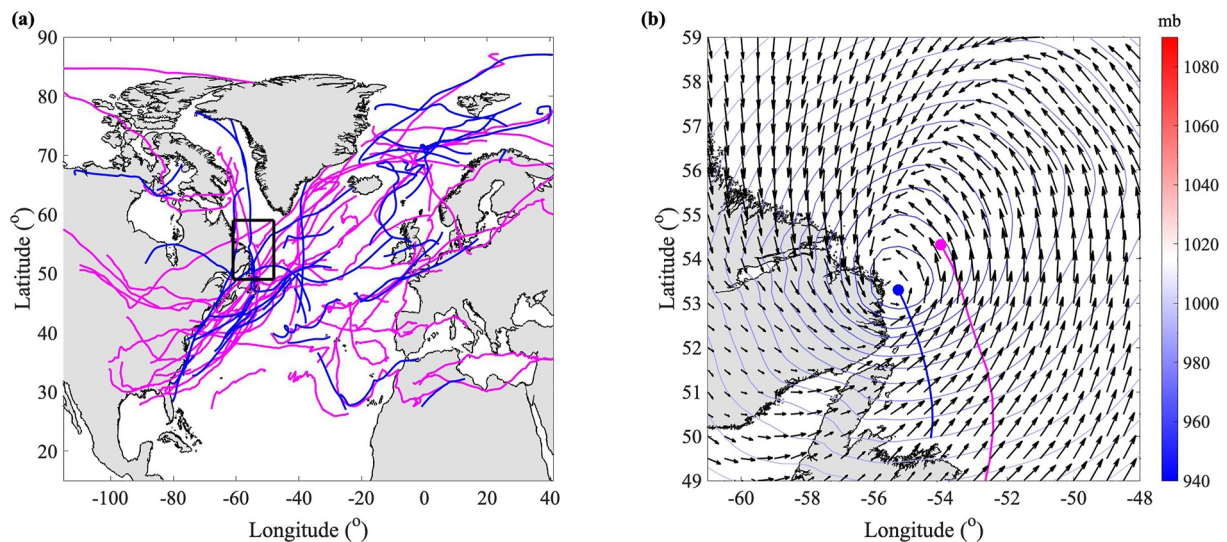
Figure 2. (a) ERA5 based EC tracks from the (Gramcianinov et al., 2020) (G20) data set, shown in magenta, and the EC tracks found in the current study, shown in blue, for the month of January in 2011. The domain of (b) is displayed as the black box in (a). (b) Two simultaneous storm tracks, with the same color convention as in (a), at 18:00 UTC on 24 January 2011. Also plotted are the ERA5 MSLP contours and U10 velocity field, of which every other vector is plotted for readability.

by both algorithms, along with the 10 m wind fields and MSLP contours from the ERA5 reanalysis. The offset between the identified cyclone centers at this time step is approximately 150 km. An animation of all the cyclone tracks shown in Figure 2, plotted along with the hourly 10 m wind fields and MSLP from the ERA5 reanalysis can be found in S2. The same tracks are also plotted over the 850 hPa level wind vectors and relative vorticity fields in S3. These animations show that the offset of tracks highlighted in Figure 2b is resulting from a systematic difference between the two tracking methods.

3.2. Extratropical Cyclone Density

In the North Atlantic high EC center density can be seen just southeast of Greenland, which aligns well with a known EC hot spot. Also visible in Figure 1 is a trail of cyclone density off the east coast of the U.S., an area where ECs form and then tend to track to the northeast (Gramcianinov et al., 2020; Neu et al., 2013; Ponce de León & Bettencourt, 2021). A similar region of high EC activity is apparent in the Northwestern Pacific off the coast of Japan, with the majority of EC tracks falling between 35° and 60°N. The configuration of land masses in the Northern Atlantic allow cyclones to exist further north than in the Pacific, evident in Figure 1 between the latitudes of 60° and 72°N. The Southern Ocean, being much less restricted by land masses, shows a circumpolar band of high cyclone center density across all longitudes in between 50° and 65–70°S, the density at any particular longitude depending on the geographical extent of Antarctica. An intense region of cyclone density can be seen to the south of Australia, which is common among many EC tracking methods (Neu et al., 2013).

Figure 3 shows the relative probability distributions of the minimum pressure and maximum wind speed per EC, taken from the ERA5 fields. Also shown are the joint probability histograms of the two variables. Comparison of the minimum pressure distributions for the northern basins shows the North Atlantic to have a slightly shifted peak, toward lower minimum pressures, indicative of more intense cyclones, than in the North Pacific. The North Atlantic also shows a slightly longer tail showing more storms that reach pressures less than 920 hPa (Figures 3c and 3f). Following accordingly, the distributions of maximum wind speed also show the North Atlantic ECs to be slightly more intense than in the Pacific (Figures 3b, 3c, 3e, and 3f).

The Southern Ocean shows much higher EC activity, having approximately twice the EC count than that of the combined northern hemisphere ocean basins. The distribution of minimum pressure centers in the Southern Ocean shows an impressive shift toward more intense lows, with most cyclones reaching between 980 and 956 hPa, and the distribution exhibiting a larger percentage of cyclones reaching pressures below 940 hPa (Figure 3g). Figure 3h shows the distribution of max winds in Southern Ocean ECs to be narrower around peak, shifted toward higher winds, centered at 21 ms⁻¹. The joint histograms for all three basins show the general
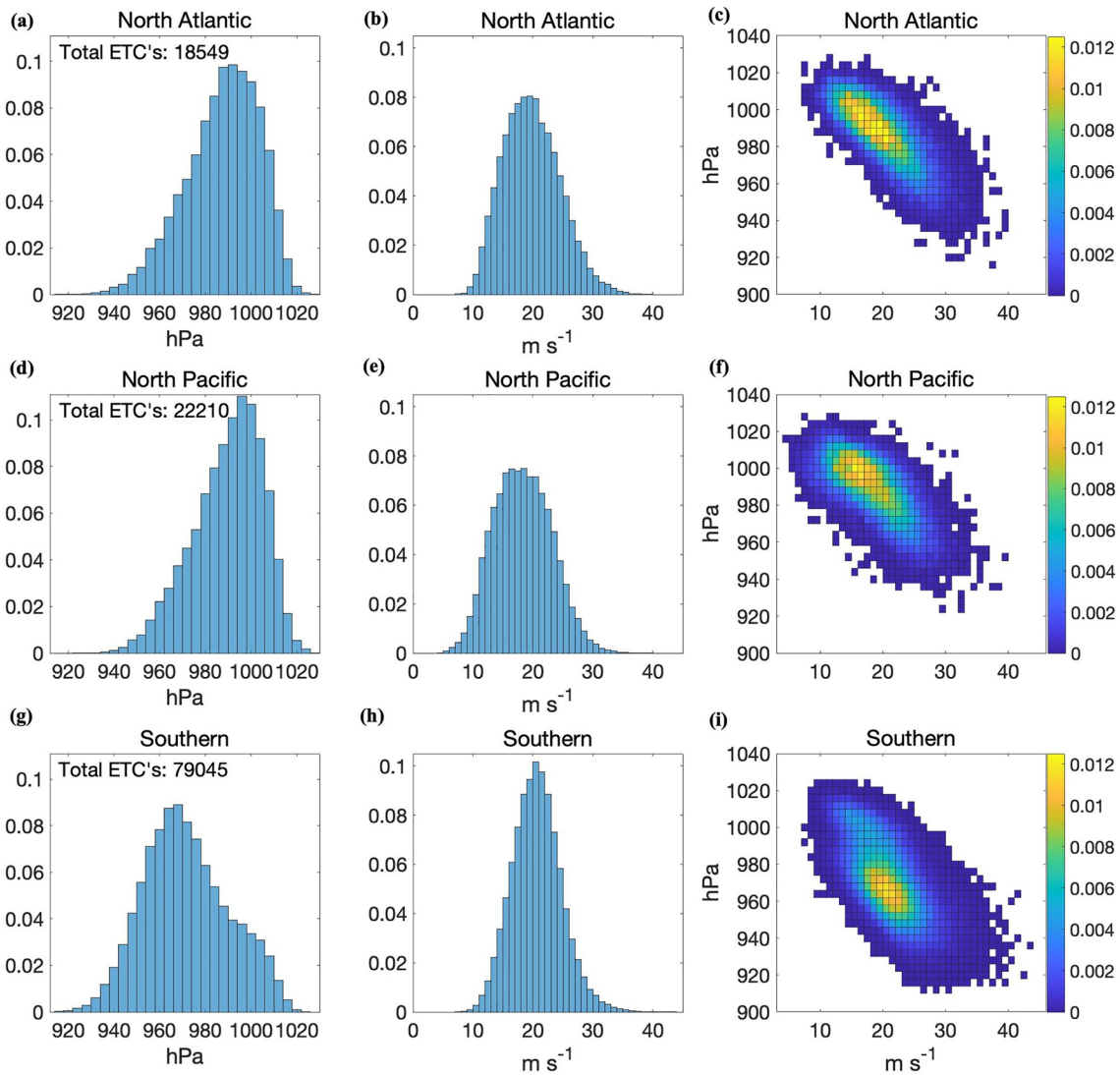
Figure 3. Relative probability histograms of the minimum pressure (a, d, and g) and maximum wind speed (b, e, and h) over the lifetime of each EC, sampled from the ERA5 fields, tracked in the North Atlantic (a and b), North Pacific (d and e), and Southern Ocean (g and c). Panels (c, f, and i) show the corresponding joint probability histograms of the minimum pressures and maximum wind speed. The total number of ECs tracked in each domain over the full 42 year period are also listed. The max wind speed per cyclone is defined as the max wind speed sampled within 500 km along the EC track.

relationship of maximum winds increasing with lower minimum pressures. Again in the Southern Ocean, the joint histogram shows a shifted peak toward coinciding higher wind speeds and lower minimum pressures, while also highlighting a higher occurrence of more extreme events (Figure 3i).

The relative probability distributions of the translational speed and deepening rate, or change in minimum pressure, for every time step along all the cyclone tracks in each basin can be seen in Figure 4. The translational cyclone velocities are calculated from positions along the filtered storm tracks described in Section 2.2. All three domains show similar distributions of cyclone velocities, with the Southern Ocean depicting a slightly wider, shifted peak toward higher EC speeds. The deepening rate distributions in Figure 4b show that the EC intensification occurring in the Northern Atlantic and Pacific to be fairly similar, however the Southern Ocean shows slightly increased intensification overall. This being evident from the smaller, broader peak depicted around zero and a tail that drops off less rapidly toward larger negative values.

Several instances of very large deepening rates up to ±10 hPa hr^{-1} in the Northern basins and ±20 hPa hr^{-1} in the Southern Ocean were excluded from Figure 4b to better represent the data in these figures, which include 99.74%, 99.8%, and 99.72% of all possible data points in the Atlantic, Pacific, and Southern Ocean basins,
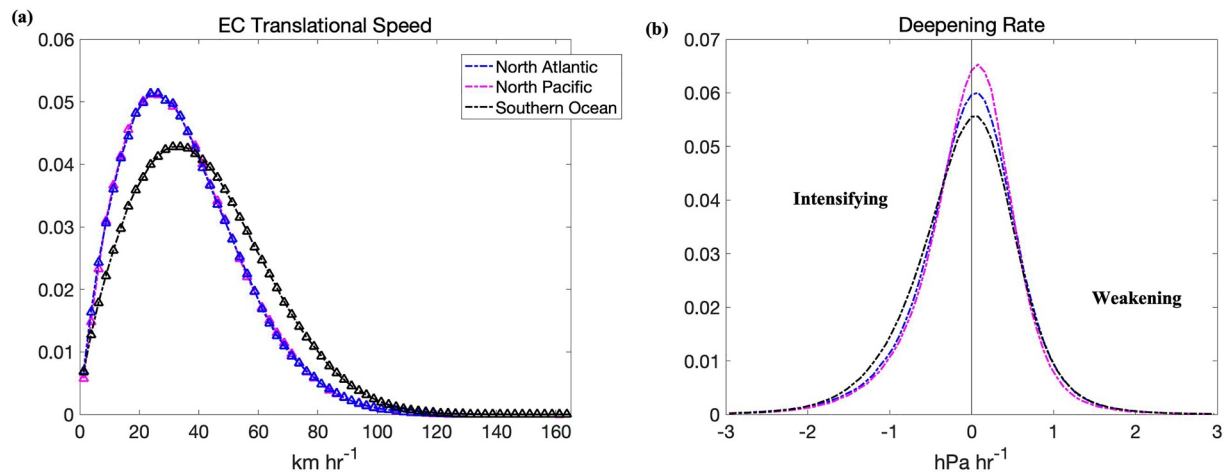
Figure 4. Relative probability distributions of (a) EC translational speed and (b) change in minimum pressure at all time steps along each EC track. Several outliers causing misleading representation of the data have been excluded in (b) accounting for 0.26%, 0.2%, and 0.28% in the Atlantic, Pacific, and Southern Ocean, respectively, of the full data sets.

respectively. Inspection of these large jumps in pressure along individual cyclone tracks suggests they are likely a result of the 12 hr data assimilation windows used in the production the ERA5 reanalysis. Pressure jumps of this magnitude can be identified at the beginning of consecutive 12 hr windows along EC tracks. While constraints are used within the analysis window to ensure smooth hourly fields, slight discontinuities have been documented in the boundary layer (e.g., 10 m winds) at these transition points (Hersbach et al., 2020). Deepening rates of up to about 2–2.5 hPa per hour have been reported in ECs using 6 hr resolution fields of MSLP (Ponce de León & Bettencourt, 2021; Rudeva & Gulev, 2011). Given the higher temporal resolution of the fields used here, it is likely that higher deepening rates could be observed, but it is difficult to say conclusively what the upper limit of deepening rates are in ECs and what large deepening rates are due this numerical artifact. Rapid intensification of cyclones, or rapid deterioration due to landfall, between assimilated observations could also exacerbate this issue.

The distribution of cyclone speeds across latitudes in each basin (Figure 5) show the largest EC speeds to occur in the mid latitudes of all three domains. Interestingly, the North Atlantic and Southern Oceans show similar distributions of speeds with a rounded peak of the fastest moving storms centered around 50° North or South with the highest distributions appearing for cyclones traveling at ~15–55 km hr^{-1} in-between 50 and 70° latitude. The same distribution shown for the Pacific shows again the influence of the land masses resulting in two peaks split around 66°–68°N, where Alaska and Eastern Russia meet in the northern region of the basin. The mid-latitude peak is also shifted slightly further equatorward compared to the other regions. The lack of land masses in the Arctic Pacific also allows for faster moving cyclones than in the poleward regions of the Atlantic and Southern
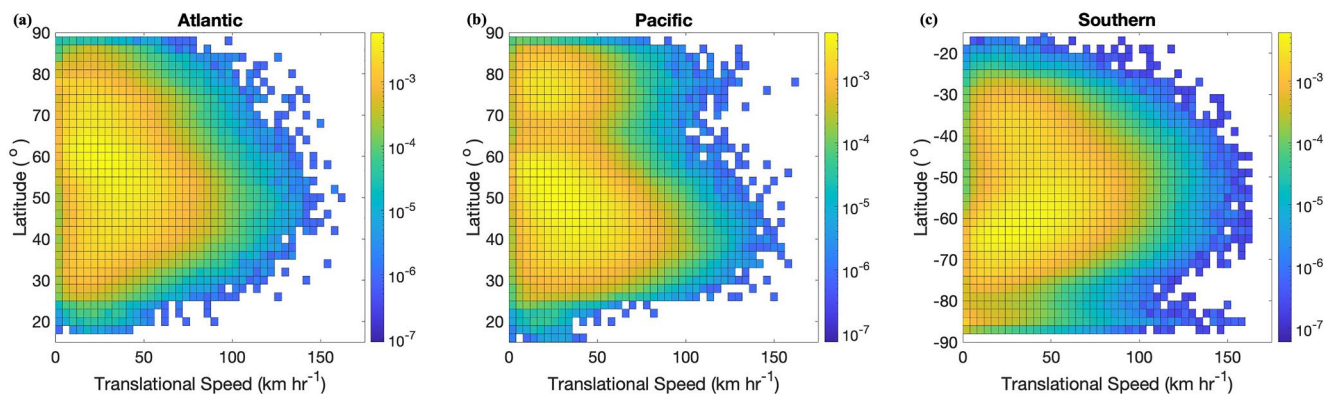

Figure 5. Joint relative probability distributions of cyclone transnational speed with degree latitude for the (a) Atlantic, (b) Pacific, and (c) Southern Oceans.
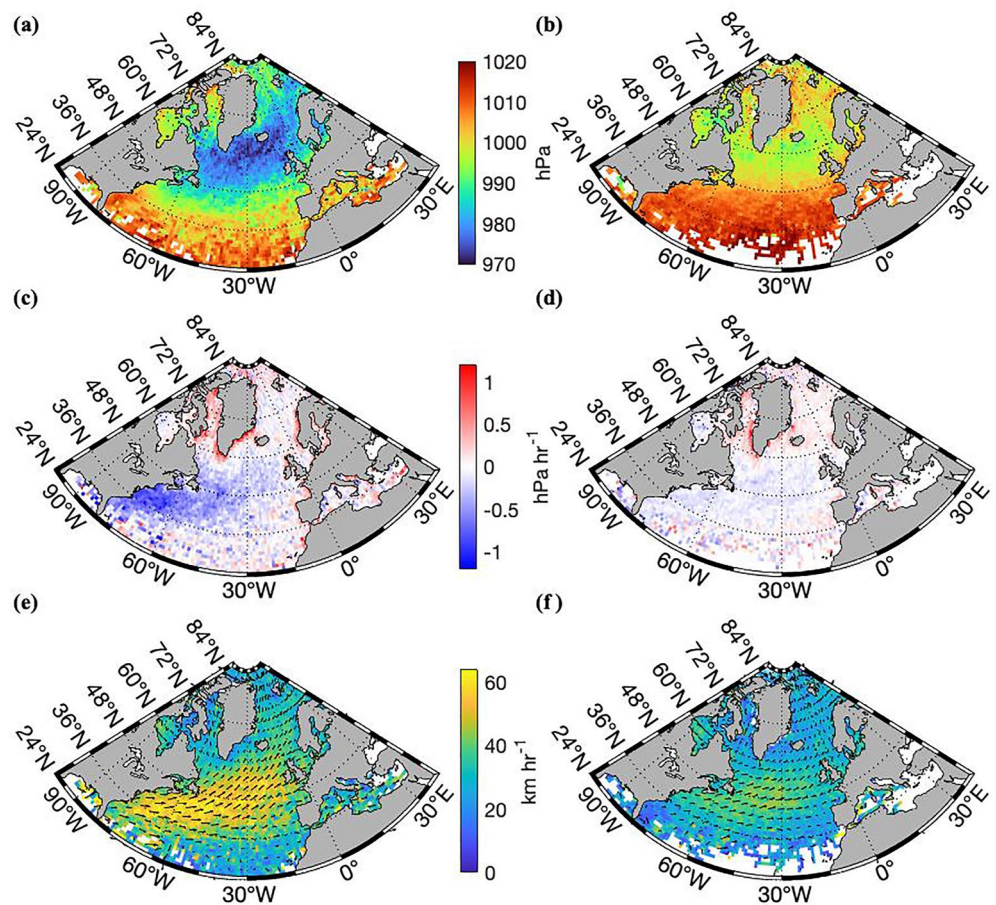
Figure 6. (a and b) Average cyclone center pressure, (c and d) average deepening rate, and (e and f) average translational velocity in 1° bins shown for (a, c, and e) northern hemisphere winter (DJF) and (b, d, and f) summer (JJA) in the North Atlantic.

Oceans. The large velocities seen south of 80°S are likely due to the chaotic nature of the cyclone centers, and modeling there of, when interacting with the large land mass of Antarctica.

Seasonal trends in average EC minimum pressure center, change in minimum pressure per hour (deepening rate), and translational velocity for the North Atlantic are shown in Figure 6. It is apparent that during the winter months (DJF), ECs on average have lower minimum pressures, quicker rates of intensification based on average decreasing minimum pressures, and faster translational velocities than during the summer months (JJA). The fastest moving cyclones also coincide spatially with the region of strongest intensification extending off the east coast of the US toward Western Europe.

Figure 7 shows similar EC trends in the North Pacific to that of the Atlantic. Both northern hemisphere basins show regions of strong deepening rates along their western boundaries, most drastically shown in the winter months, but still visible during the summer. Also visible in both domains are regions of strong cyclone decay, shown in red on the color map in Figures 6c, 6d, 7c, and 7d, in the Northern regions where cyclones circulation is disrupted, at least in lower atmospheric levels, as they travel over land masses. The Southern Ocean seasonal EC trends (Figure 8) show the same patterns as observed in the northern hemisphere, albeit with less variation from winter to summer. The lack of land masses in the southern hemisphere results in a circumpolar region of the lowest average minimum pressures, highest intensification rates, and fastest velocities, wrapping almost entirely around Antarctica. A relative minimum is observed where the tips of South Africa and Antarctica create a blocking point and strong EC weakening occurs along their western coasts (Figure 8). Table 1 lists the annual average number of storms per basin, as well as the seasonal averages over the 42 year period.
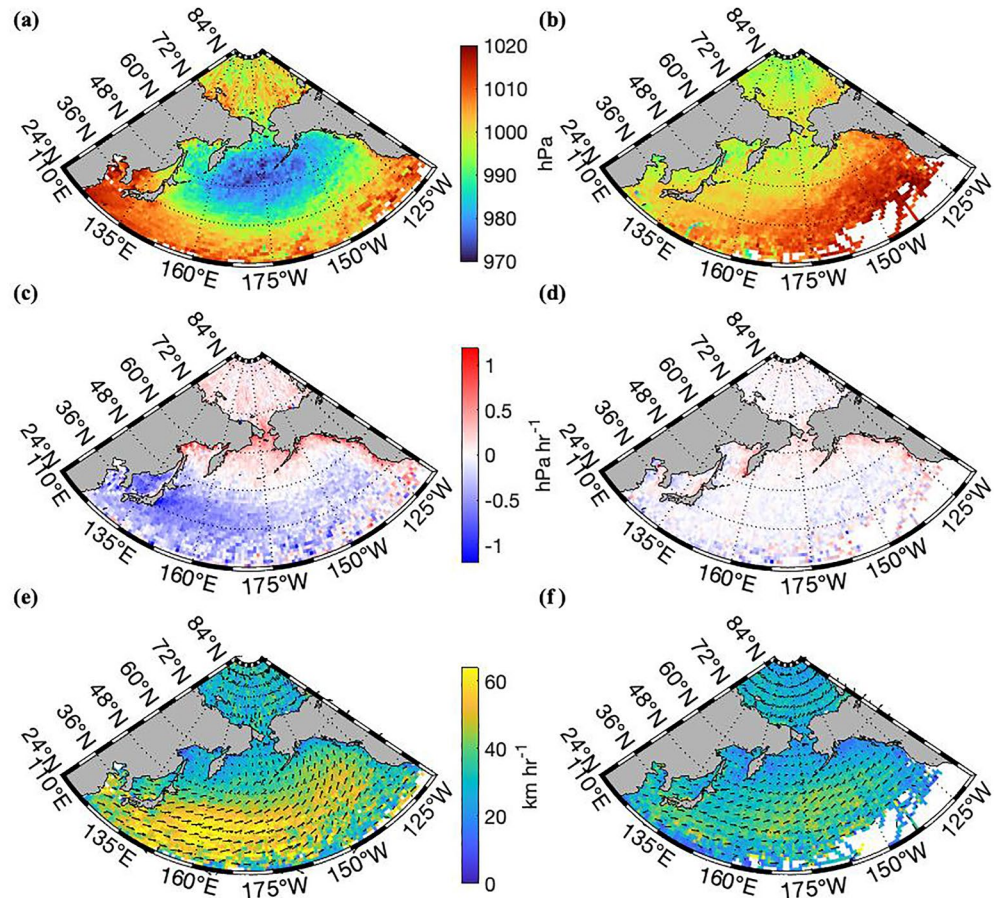
Figure 7. (a and b) Average cyclone center pressure, (c and d) average deepening rate, and (e and f) average translational velocity in 1° bins shown for (a, c, and e) northern hemisphere winter (DJF) and (b, d, and f) summer (JJA) in the North Pacific.

3.3. Climatology of H_s Under Extratropical Cyclones

Figure 9a shows the global average H_s within 500 km of EC centers during northern hemisphere winter (DJF). As extensively proven effective by Timmermans et al. (2020), Young and Donelan (2018), Takbash et al. (2019), and Young et al. (2020), we use 2° × 2° bins to plot the satellite based altimeter data in order to reduce the effect of preferential sampling along satellite tracks. The regional maximum of average wave heights can be seen in the center of the North Pacific, just south of the Bering Sea, while the North Atlantic maximum wave heights lie relatively further to the northeast in the basin. Figure 9b shows the same global cyclone induced average H_s for the southern hemisphere winter (JJA). Following the seasonal trends of ECs seen in Figures 6–8, seasonal changes in the Southern Ocean wave heights are much less extreme than that of northern hemisphere regions. Interestingly, the North Atlantic shows the most intense region, and also the largest averages, of H_s observed in any basin.

Figures 10a–10c show the cyclone center density, average translational velocity, and average associated H_s for deep cyclones. Deep cyclones are defined here as instances when the minimum pressure of an EC is below 980(960) hPa in the northern (southern) hemisphere. The threshold in the southern hemisphere has been set to correspond to the tendency of southern hemisphere ECs to be deeper overall. Similar thresholding has been used by Neu et al. (2013) and Rudeva and Gulev (2011) to explore deep cyclones. Under these more intense cyclones we see average significant wave heights much larger than that of the climatological mean preferentially distributed on the equator-ward regions of all basins, while relative minimums are present toward the poles. Average cyclone velocities are also shown to decrease poleward (Figure 10b).

To investigate mean wave height with increasing EC intensity, we bin H_s observations within 4 different max wind thresholds, shown in Figure 11. The maximum wind speed for this portion of the analysis is determined at
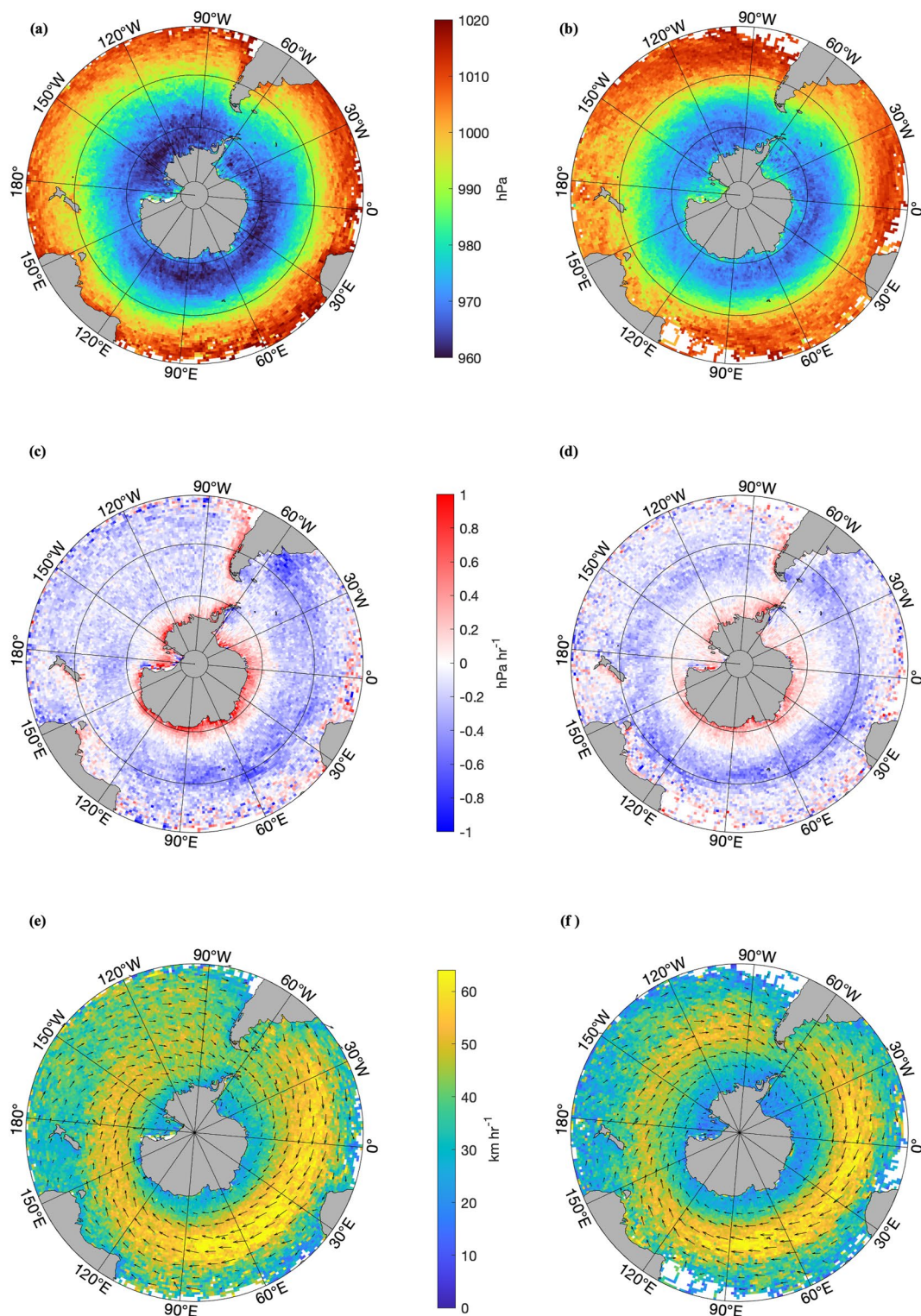
Figure 8. Average cyclone center pressure (a and b), (c and d) average deepening rate, and (e and f) average translational velocity in 1° bins shown for (a, c, and e) southern hemisphere winter (JJA) and (b, d, and f) summer (DJF) in the Southern Ocean. Lines of latitude are on the same intervals shown in Figure 1.

Table 1
Annual and Seasonal Number of Cyclones Tracked per Year Averaged Over the 42 Year Period

Basin	Total	DJF	MAM	JJA	SON
North Atlantic	441.6 ± 23.7	129.7 ± 10.9	113.0 ± 10.2	84.5 ± 9.6	114.4 ± 9.2
North Pacific	528.8 ± 25.5	153.2 ± 10.9	130.5 ± 9.4	112.1 ± 12.3	133.0 ± 10.3
Southern	1882.0 ± 54.0	384.2 ± 21.7	486.1 ± 19.6	535.4 ± 21.8	476.3 ± 21.0

Note. Cyclones are seasonally binned based on the first time step of their track. Ranges listed in the table show plus or minus one standard deviation.

every time step along the EC tracks, again within 500 km of each EC center, and assigned to all the corresponding H_s at that time step if any exists. During weaker cyclone instances with max winds less than 12 m s⁻¹, we observe relative small wave climates with average H_s on the order of about 1–3 m, although the Southern Ocean still exhibits slightly larger waves than the northern basins. We see a similar result for max winds ranging from 12 to 18 m s⁻¹, with the southern ocean reaching higher average H_s up to about 4–5 m. Under max wind speed between 18 and 24 m s⁻¹ hot spot regions of large waves in the Northeast Atlantic and Northern region of the Pacific, are more prominent. The Southern Ocean shows a band of large waves under this wind regime varying between 45° and 60°S. ECs with maximum winds above 24 m s⁻¹ show average H_s up to 8 m in all three regions. The coverage of data available above this wind threshold, shown in Figure 11d, also reveals that ECs with winds of this magnitude tend to exist further poleward than weaker cyclones.

The relationship between cyclone translational speed and average wave height, seen in Figure 12, shows similar trends to that of EC maximum wind speed, but shows less variability across thresholds. Interestingly, the maps of average H_s under ECs traveling slower than 25 km hr⁻¹ and those traveling between 25 and 50 km hr⁻¹ do not vary greatly, and in some regions the slower cyclones (Figure 12a) produce slightly higher average wave states, most notably in the region to the southeast of Greenland in the North Atlantic. In the Southern Ocean a similar band of large wave heights can be seen wrapping around the southern hemisphere with a minimum just to the east of South America, where the atmospheric westerly flow is constricted by the tips of South America and Antarctica on either side of the region of ocean known as Drake's Passage. The region just to the east of Southern America is a well known cyclone genesis region limited to young cyclones, traveling at a large variety of speeds, with inadequate fetch to produce large waves in the immediate region. This is also evident in the average H_s seen in the region in Figure 11. Regions with similar characteristics include the east coast of the United stated and Western pacific south of Japan (Figures 11 and 12). Cyclone speeds in the higher ranges are associated with elevated average wave climates. In the northern hemisphere, the largest wave heights, as they relate to cyclone speeds, are concentrated to the north/northeast in each basin. The Southern Ocean is much less spatially constricted with fast moving cyclones creating larger waves from the tip of Africa to the tip of South America as they travel along the westerly moving atmospheric circulation. On average the largest waves are created by the fastest moving cyclones, the extent of which can also be seen in the spatial coverage of wave data in Figure 12.

3.4. Influence of North Atlantic Oscillation

Figures 13a, 13c, 13e and 13b, 13d, 13f show average EC characteristics during winter months (DJF) coinciding with monthly indexed positive and negative phases of NAO, respectively. The NAO index used here is calculated by the NOAA Climate Prediction Center using the Rotated Principal Component Analysis (RPCA) from Barnston and Livezey (1987).

Larger winter cyclone velocities can be seen in the North Atlantic during positive NAO extending from the east coast of the US to the northeast,
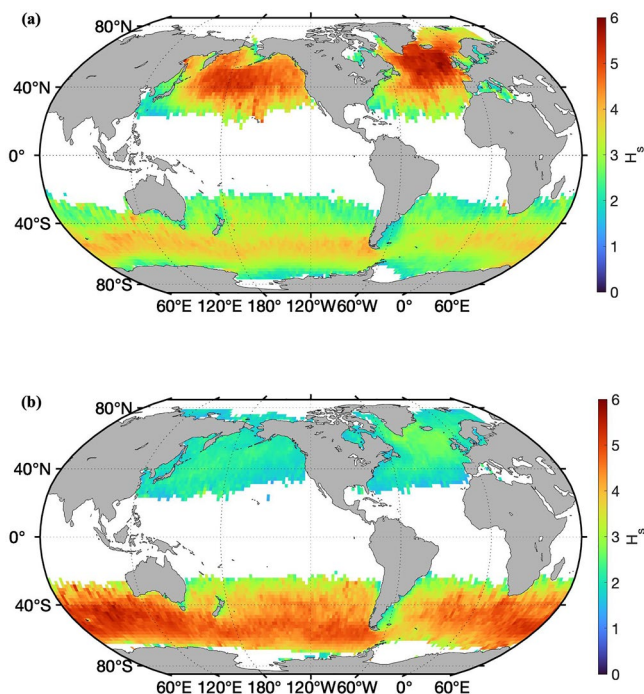

Figure 9. 2° × 2° latitude/longitude bins of average H_s sampled within 500 km of EC centers over the period of 1985–2020 for (a) northern hemisphere winter (DJF) and (b) southern hemisphere winter (JJA). Bins with less than 100 data points, approximately 1% of the average bin size when considering all H_s data, are excluded from all H_s related figures.
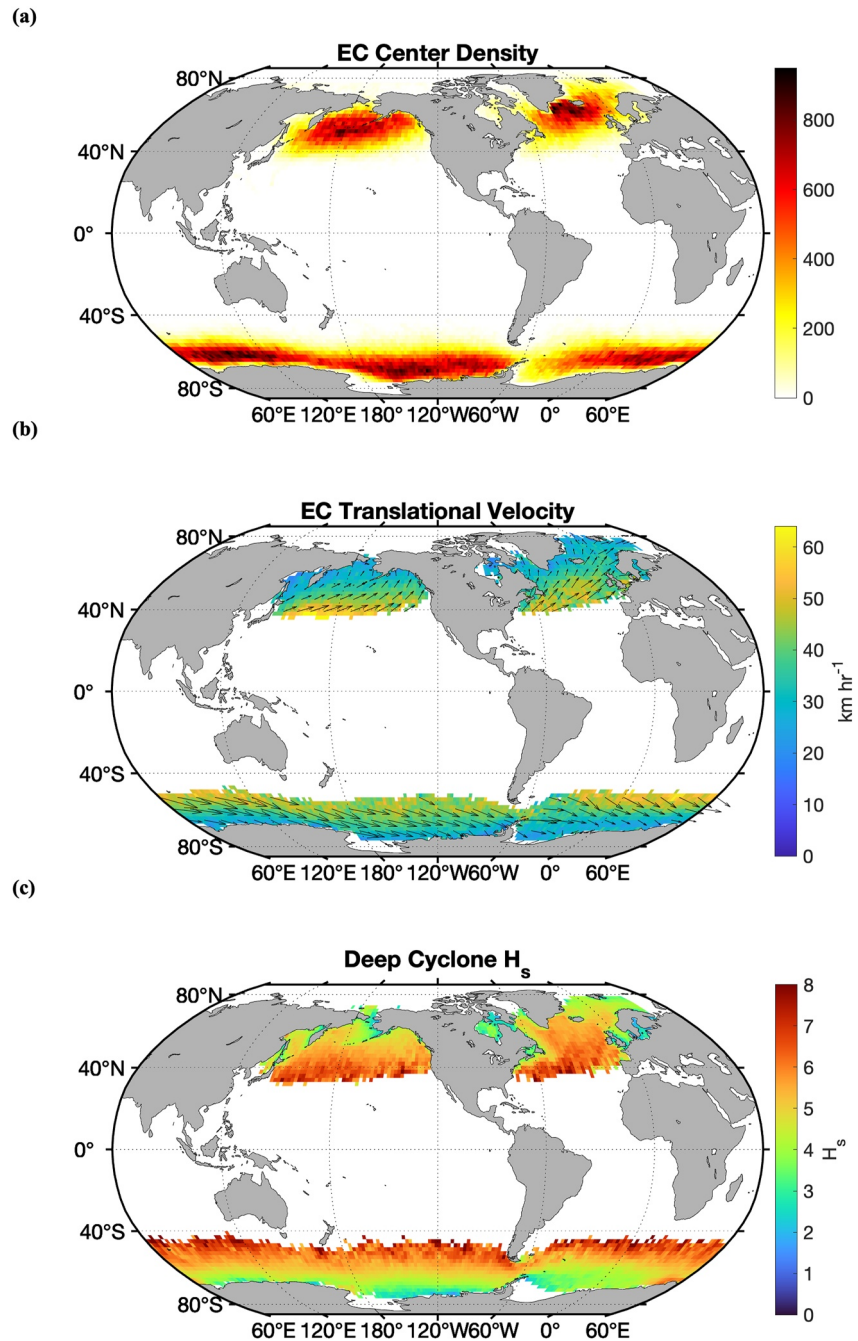
(a)

(b)

(c)

Figure 10. Climatology for deep ECs, defined as EC instances when cyclone minimum pressure is less than or equal to 980 hPa in the northern hemisphere and 960 hPa in the southern hemisphere. Panel (a) shows the total count of deep EC center occurrence through out the entire time period (1979–2020), (b) shows the average translational velocity of the ECs, and (c) shows the average H_s again sampled within 500 km of deep EC centers during the time period of available satellite measurements (1985–2020). $2° \times 2°$ latitude/longitude bins are used for (a–c).

funneling cyclones in between Western Europe and Greenland. During the negative mode these velocities are strongly subdued on the eastern half of the North Atlantic, but however appear slightly increased just off the US east coast (Figures 13a and 13b). The cyclone center density plots show a shift of cyclone activity generally from the Northwestern Atlantic during the negative phase to the Northeastern Atlantic during the positive phase. The cyclone center density is also enhanced and more organized during positive NAO (Figures 13c and 13d). On
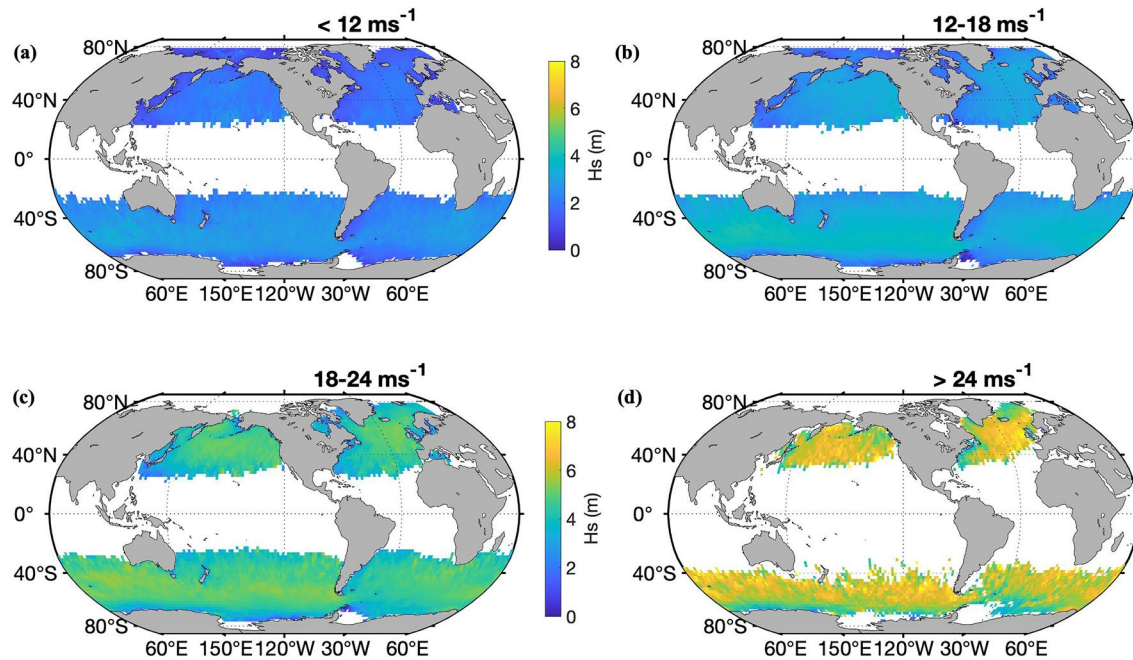
Figure 11. Average H_s data binned with varying EC maximum wind speeds. Maximum wind speeds are calculated from the ERA5 wind fields within 500 km of each cyclone center at every time step. H_s data are binned spatially in 2° latitude/longitude bins. Maximum wind thresholds for each plot are listed.

average cyclones are more intense, reaching lower minimum pressures, during positive NAO with the strongest cyclones occurring in the region inside 54°–66°N and 40°W to 0° (Figures 13e and 13f). The strongest average EC region associated with the negative NAO phase is notably less extreme but also shifted toward the western half of the basin, resulting in slightly stronger average minimum pressures reaching the Northeastern US and Eastern Canada. Figure 14 shows a composite analysis of observed H_s within the same winter ECs during positive and negative NAO. A very similar enhancement and shift in largest average wave heights can be seen in the
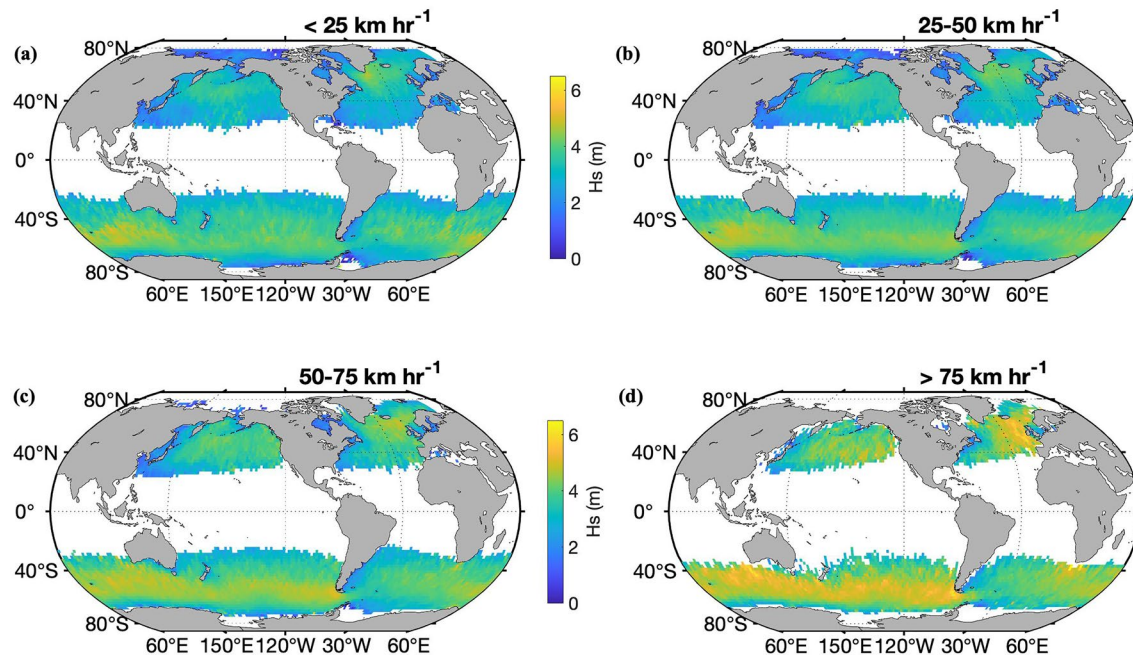

Figure 12. Average H_s data binned by increasing EC translational speed. EC speed criteria are listed in each plot and H_s are binned spatially in the same 2° bins as Figures 9 and 11.
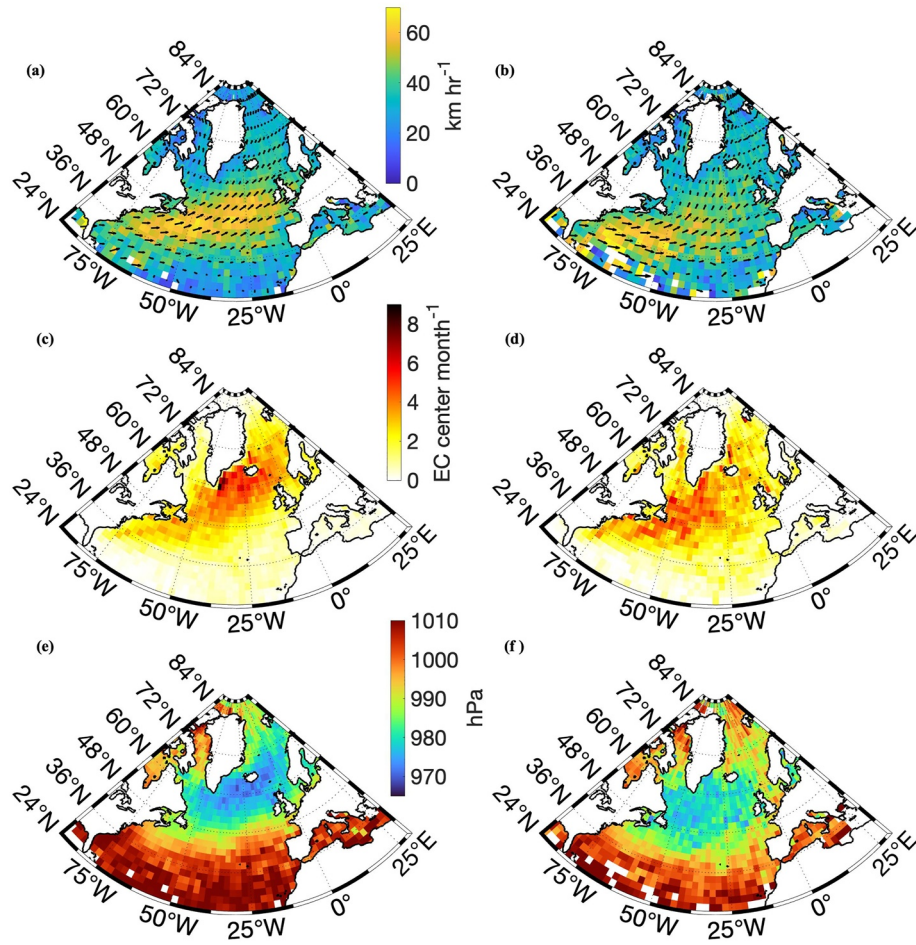
Figure 13. Average winter (DJF) cyclone characteristics in the North Atlantic during positive (a, c, and e) and negative (b, d, and f) modes of the NAO. Panels (a and b) show the average cyclone translational velocity, (c and d) show the cyclone center density normalized by number of months identified as positive or negative NAO phase during the 42 year study period, and (e and f) show the average cyclone center minimum pressure per bin.
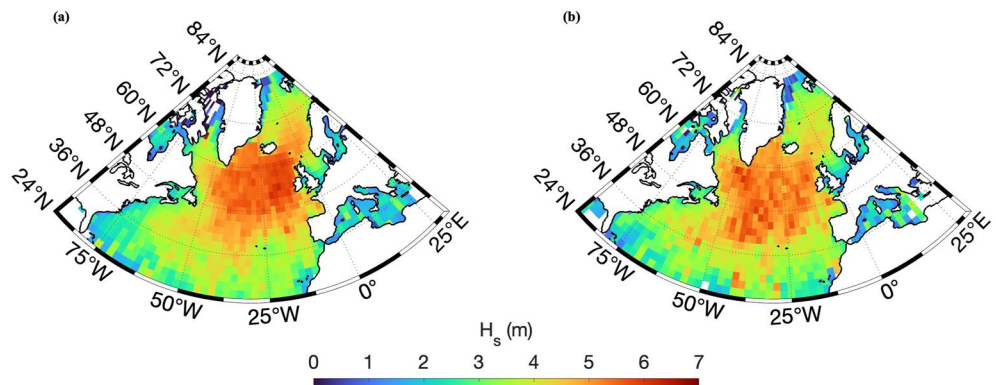

Figure 14. Average H_s sampled within 500 km of winter (DJF) ECs during (a) positive and (b) negative phases of the NAO. Data is binned and averaged in 2° latitude/longitude bins.

positive NAO, EC-induced H_s fields. During the negative NAO phase, the largest bin averages appear less organized and shifted again toward the Northeast US coast and Eastern Canada.

4. Discussion

4.1. Extratropical Cyclone Tracker Comparison

Here we contrast our tracker with the method of G20, which is described in detail by Hoskins and Hodges (2002) and Hoskins and Hodges (2005). From S2 and S3, along with Figure 2, it is apparent that the cyclone tracker presented here is more adept at identifying cyclone centers with respect to the ERA5 10 m and 850 hPa wind fields than that of G20. In order to identify cyclone centers in the noisy relative vorticity field, G20 spectrally filters the vorticity and tapers the spectral coefficients to smooth the data. Large-scale atmospheric features are also removed by setting zonal wavenumbers in the spectral representation of the field ≤5 to zero. Using the resulting fields, G20 is able to detect smaller scale cyclones and detect cyclones earlier in their development stage, as seen in S2, where MSLP dependent methods will only identify systems once more development or intensification occurs (Gramcianinov et al., 2020; Sinclair, 1994). However, G20 shifts the identified cyclone centers in space compared to the original ERA5 850 hPa wind and relative vorticity fields, as well as the MSLP and 10 winds fields, evident in S2, S3, and Figure 2. Spatial differences between cyclone centers identified by our method and G20 are on the order of 100 km which can have a large effect when collecting wave data within a given radius of each cyclone. Because one of the main interests here is also future study of the complex relationship of wind-wave orientation and interaction within varying EC sectors, the skill of accurately defining cyclone centers is imperative. Thus our method is more appropriate for our application.

Comparing the average total cyclone count in the North Atlantic between our method and G20 is possible due to similar thresholds put in place by both methods and similar domains explored. On average the tracking and detection method used here identifies 20% less cyclones than that of G20 annually. This however fluctuates between 28% in the summer months and 17% in the winter months, showing the tendency for G20 to be more skilled at detected weaker summertime cyclones. Qualitatively, cyclone center density maps from either method show fairly consistent spatial patterns. This result is similar to that found by Greeves et al. (2007) who applied the method of Hoskins and Hodges (2002) to MSLP and 850 hPa relative vorticity fields, finding agreement in spatial patterns with magnitudes 20%–50% lower for the cyclone tracks derived from MSLP (Greeves et al., 2007; Ulbrich et al., 2009).

(Neu et al., 2013) compiled the results of commonly used cyclone trackers. Binning the minimum pressures of each cyclone detected in 10 hPa intervals, they found the 1,000–1,010 hPa bin to contain the largest percentage of cyclones for the Northern Hemisphere. Figures 3a and 3b show that the distribution of minimum cyclone pressures in the Northern Hemisphere peak below 1,000 hPa, indicating that the lower total number of cyclones detected here is due to the limitation of tracking smaller scale, weaker ECs. Ponce de León and Bettencourt (2021) show a similar peak in minimum pressure distribution at 990 hPa after selecting a subset of ECs which met criteria ensuring each system had an affect on the wavefield. A similar trend of detecting relatively less weaker ECs can be seen in the Southern Hemisphere when comparing distributions of minimum cyclone pressures between this study and Neu et al. (2013).

Neu et al. (2013) shows the wide range of results for total cyclone count in the Northern and Southern Hemispheres from various cyclone tracking methods. The authors highlight that seasonal cycles can vary quite significantly from one method to another, with trends being flipped in some cases, with trackers producing 50% more ECs during summer months than winter. Due to differences in empirical cyclone thresholds including minimum lifespan, distance traveled, and minimum intensity reached (Blender et al., 1997; Pinto et al., 2005; M. C. Serreze et al., 1997; Trigo et al., 1999; Ulbrich et al., 2009), certain trackers may detect many shallow cyclones, which include summertime heat lows. Differences in spatial and temporal resolutions of reanalysis fields used Neu et al. (2013) and the current work also adds to the difficulty of making one to one comparisons between methods.

4.2. Seasonal Trends of Extratropical Cyclones and Subsequent H_s

Seasonal changes in the large scale circulation drive the changes we observe in EC characteristics from winter to summer. In the northern hemisphere the tropospheric jet stream and baroclinic wave instabilities that cause

cyclogenesis are most intense when the latitudinal temperature gradient across the mid-latitudes are at their strongest (i.e., during the winter months) (Wallace & Hobbs, 2006). A region of particularly strong meridional temperature gradient exist along the eastern coast of North America due to the warm water transported from the tropics northwards by the Gulf Stream (Nelson & He, 2012). This region is highlighted in Figure 6c where the strongest EC intensification occurs. Similar regions can be seen in the West Pacific in Figure 7c along the coast of Japan, as well as in the Southern Ocean in Figure 8c along the southeast coast of South America, which is of course most intense during the southern hemisphere winter months (JJA). These areas of high cyclogenesis in the North Atlantic and Southern Ocean are also identified by Gramcianinov et al. (2020) and Gramcianinov et al. (2019). Cyclone translational speeds are also intensified by the stronger atmospheric large scale flow typically observed during the cold months for each hemisphere. These favorable conditions for cyclogenesis and intensification also result in the lower minimum pressures seen in Figures 6a, 7a, and 8a.

The seasonal global averages of H_s sampled only within ECs presented here are very similar to that of previous studies that have used satellite altimeter data sets to consider the full global climatology of H_s (Timmermans et al., 2020; Young et al., 2020). Seasonal averages of satellite derived H_s calculated using the European Space Agency (ESA) Climate Change Initiate for Sea State (CCI) data set, results in qualitatively equivalent spatial patterns in the mid to high latitudes as shown here in Figure 9 (Timmermans et al., 2020). Comparatively, regions of the globe with the most intense wave heights typically appear to cover a wider area and reach slightly higher averages in the EC dependent case. The Southern Hemisphere July climatology presented by Young et al. (2020) depicts a region of maximum H_s south of the Indian Ocean and a region of minimum wave heights just east of the tip of South America, which are features also seen in the JJA average here. These matching spatial patterns indicate that the mid-latitude wave climates are indeed dominated by ECs, and shows the cyclone tracker here to be well equipped at identifying cyclones with significant effects on the wavefield.

Interestingly Timmermans et al. (2020) showed H_s climatologies produced using the ESA data set to vary significantly, in certain regions, from that calculated using the Ribal and Young (2019) database. Most of these regions of large disagreement exist in smaller seas (i.e., The Gulf of Mexico, Mediterranean Sea, and Sea of Japan). The larger basins which are of focus in this paper, only show small deviation (less than 2.5%) between these data sets which have many satellite missions and much of their overall time span in common. This does show however that extra attention may be needed to resolve these issues when considering wave measurements under cyclones in high error regions.

4.3. Deep Extratropical Cyclone Wave Development

The composite of wave measurements sampled during deep cyclones (Figure 10c) shows a large scale view of the regional dependency of wave development within strong ECs. In the North Atlantic, the largest waves under deep ECs are generated in the south and southeast regions of the basin. These intense cyclones generally track from the east coast of the US toward Iceland and Western Europe, evident in Figure 10b. As Ponce de León and Bettencourt (2021) and Ponce de León and Guedes Soares (2014) have shown the largest wave development in ECs occur in the back and right hand sectors of these cyclones relative to the their direction of motion defined at the EC center. Figure 10 shows that the region of large H_s (up to 8 m) recorded in the North Atlantic is a result of this region being preferentially exposed to the large wave producing cyclone regions, where wind direction and direction of cyclone motion align. This alignment causes a phenomena often referred to as a dynamic, or extended, fetch where the movement of the storm in the propagation direction of the waves results in a larger effective area and duration over which the strong EC winds inject energy into the wavefield (Collins et al., 2021; Kita et al., 2018; Ponce de León & Bettencourt, 2021; Young & Vinoth, 2013). The Northwest portion of the basin, being more often exposed to the left sector of the deep ECs, shows relatively smaller average wave heights. Counter to having an extended fetch, the left sector of ECs exhibit wind and wave directions opposite the direction of cyclone motion, resulting in a reduced fetch as the ECs travel away from the propagating waves in the incident field (Field & Wood, 2007; Young & Vinoth, 2013).

The cyclone velocities in the North Pacific, also shown in Figure 10b, and the similar extent of large H_s observed under deep cyclones show the same effects of varied wind-wave orientations within different EC sectors. The Southern Ocean, having cyclonic flow which circulates clockwise due to the change in sign of the Coriolis force, contains ECs which exhibit extended fetches in their back and left sectors, again defined relative to their direction of motion. As cyclones in the Southern Ocean travel in a circumpolar orientation, as seen in Figure 10b, the effect

of extended fetch on the left side of the ECs results in a band of the largest H_s under deep cyclones wrapping around the globe between approximately 45° and 55°S. Moving south from this band of extreme wave heights we again observe the effect of opposing wind and cyclone direction resulting in limited wave growth on the right side of ECs in the Southern Ocean. Of course, because this analysis is confined to EC driven wave development, it is important to note that large waves on the same order of magnitude can also exist in the tropics and subtropics due to tropical cyclones.

Regions of the largest average waves heights under fast moving ECs and those with the highest wind speeds, seen in Figures 11d and 12d, respectively, largely overlap with these highlighted regions of extended fetch in each basin. Cases of extreme wave growth have been linked to the synchronization of storm and wave velocities, which results in trapped-fetch waves. This resonance effect can create exceptionally large waves due to their increased exposure to strong atmospheric forcing (Bowyer & MacAfee, 2005). The tendency for larger wave heights with increased cyclone velocity is also evident by the poleward decrease of velocities and average wave heights seen in Figures 10b and 10c. Interestingly, the average velocity of deep cyclones in all three regions show these storms travel with a stronger poleward velocity component compared to the seasonal averages shown in Figures 6–8.

4.4. NAO

The trends seen in the North Atlantic during the positive and negative phases of the NAO are in good agreement with trends previously observed (Pinto et al., 2009; M. C. Serreze et al., 1997; Wang, Wan, & Swail, 2006). The effects of regional EC dependence of wave growth are also highlighted during the positive phase of the NAO. Based on the EC density and average velocity, shown in Figures 13a and 13c and the corresponding H_s in Figure 14a, we observe the highest average waves in the region to the east and southeast of the densest EC activity, again showing evidence of enhanced wave growth in the right sector of ECs. The stronger ECs observed during the positive NAO create very large waves, impacting to coastlines of Western Europe. The shift of stronger ECs toward the east coast of North America during the negative phase of NAO has also been documented by Chartrand and Pausata (2020), which reports negative NAO being associated with roughly twice as many heavy snow producing storms over the region covering Nova Scotia, New England, and the Mid-Atlantic. This is attributed to the increase in cyclogenesis of coastal cyclones along the US East coast and southward shift of storm tracks observed during negative NAO.

Cyclone velocities are also weakened in the North Atlantic during negative NAO, with a small exception being off the coast of the US where cyclones speed is seen to increase slightly. The weakened dipole made up of the Icelandic Low and Azores High during the negative phase results in a weakened jet stream, resulting in a blocking effect of cyclones traveling to the northeast toward Western Europe (Marshall et al., 2001). The decreased velocities of these overall weaker cyclones correspond to smaller average H_s in the region (Figures 13 and 14).

5. Conclusion

The new approach to tracking ECs displayed here is well adapted to efficiently and accurately locate cyclones centers in state of the art reanalysis products with finer scale spatial and temporal resolution. Leveraging existing image processing tools allows for less spurious identification of potential low pressure centers than previous MSLP-based methods. The use of MSLP fields instead of relative vorticity can cause shorter lived and weaker cyclones to go undetected, however we've shown our approach results in more precise assignment of cyclone centers relative to the high resolution wind fields of the reanalysis used.

Using this 42 year database of EC tracks we investigate seasonal and longer-term regional trends in EC density, characteristics, and their average effects on the wave fields they traverse. We find increased cyclone intensification, average translational velocity, and overall storm count in all regions during their respectively winter seasons. Shifting modes of the NAO are also shown to have basin wide effects on EC characteristics and density which then translate to the associated wave heights observed. Using satellite altimeter observations we show these EC characteristics have a direct effect on wave generation, possibly the most interesting relationship being that of cyclone velocity and increased wave heights. Overall patterns of EC-induced wave heights closely resemble climatic patterns in Timmermans et al. (2020) and Young et al. (2020), revealing the dominance of these storms in the global wave climate. Analysis of waves in deep cyclones reveal the need for further investigation

of cyclone region dependent wave generation and effects of wave-storm resonance induced by the extended fetch phenomenon.

It should be noted that this EC tracking algorithm, being designed for the purpose of studying waves under EC conditions, is less suited for studying climate processes where smaller scale ECs are likely very important in the latitudinal atmospheric exchanges of heat, momentum, and moisture. With this limitation taken into consideration, this collection of EC tracks is better equipped for the future detailed investigation of wind-wave orientation and its affect on wave growth in different EC sectors. Using this data set of EC tracks, future work involves the investigation of wave measurements in a cyclone centered reference frame, along with in-depth analyses of dynamic fetch and its potential to create extreme sea states.

Data Availability Statement

The ERA5 reanalysis is available directly from the Copernicus Climate Change Service (C3S) Climate Date Store (https://cds.climate.copernicus.eu/#!/search?text=ERA5&type=dataset, Hersbach et al., 2020). The Satellite Radar Altimeter data can be accessed through the ongoing IMOS (Integrated Marine Observing System) Surface Waves Sub-Facility Altimeter Wave/Wind database which is available through the Australian Ocean Data Network portal (AODN: https://portal.aodn.org.au/, Ribal & Young, 2019). EC tracks derived from the ERA5 reanalysis by Gramcianinov et al. (2020) are available for download at https://data.mendeley.com/datasets/kwcvfr52hp/1. NAO indexes from the NOAA Climate Prediction Center can be found at https://www.cpc.ncep.noaa.gov/products/precip/CWlink/pna/nao.shtml (NOAA/National Weather Service, 2022). True color satellite images from the VIIRS/NPP satellite can be found at https://neo.gsfc.nasa.gov/ (NASA Earth Observations, 2022). The cyclone tracking algorithm and cyclone track position data used to produce the figures here can be found at https://github.com/jlodise/JGR2022_ExtratropicalCycloneTracker.

References

Abdalla, S., Janssen, P. A., & Bidlot, J. R. (2010). Jason-2 OGDR wind and wave products: Monitoring, validation and assimilation. *Marine Geodesy*, *33*(S1), 239–255. https://doi.org/10.1080/01490419.2010.487798

Alves, J. H. G., & Young, I. R. (2003). On estimating extreme wave heights using combined Geosat, Topex/Poseidon and ERS-1 altimeter data. *Applied Ocean Research*, *25*(4), 167–186. https://doi.org/10.1016/j.apor.2004.01.002

Barnston, A. G., & Livezey, R. E. (1987). Classification, seasonality, and persistence of low-frequency atmospheric circulation patterns. *Monthly Weather Review*, *115*(6), 1083–1126. https://doi.org/10.1175/1520-0493(1987)115<1083:csapol>2.0.co;2

Bernhardt, J. E., & DeGaetano, A. T. (2012). Meteorological factors affecting the speed of movement and related impacts of extratropical cyclones along the U.S. East Coast. *Natural Hazards*, *61*(3), 1463–1472. https://doi.org/10.1007/S11069-011-0078-0/FIGURES/7

Black, P. G., D'Asaro, E. A., Drennan, W. M., French, J. R., Niiler, P. P., Sanford, T. B., et al. (2007). Air-sea exchange in hurricanes. *Bulletin of the American Meteorological Society*, *88*(3), 357–374. https://doi.org/10.1175/bams-88-3-357

Blender, R., Fraedrich, K., & Lunkeit, F. (1997). Identification of cyclone-track regimes in the North Atlantic. *Quarterly Journal of the Royal Meteorological Society*, *123*(539), 727–741. https://doi.org/10.1002/qj.49712353910

Bowyer, P. J., & MacAfee, A. W. (2005). The theory of trapped-fetch waves with tropical cyclones—An operational perspective. *Weather and Forecasting*, *20*(3), 229–244. https://doi.org/10.1175/WAF849.1

Chartrand, J., & Pausata, F. S. R. (2020). Impacts of the North Atlantic Oscillation on winter precipitations and storm track variability in southeast Canada and the northeast United States. *Weather and Climate Dynamics*, *1*(2), 731–744. https://doi.org/10.5194/wcd-1-731-2020

Collins, C., & Hesser, T. (2021). *altWIZ: A system for satellite radar altimeter evaluation of modeled wave heights* (Technical Report). US Army Engineer Research and Development Center.

Collins, C., Hesser, T., Rogowski, P., & Merrifield, S. (2021). Altimeter observations of tropical cyclone-generated sea states: Spatial analysis and operational hindcast evaluation. *Journal of Marine Science and Engineering*, *9*(2), 1–31. https://doi.org/10.3390/jmse9020216

Donelan, M. A., Drennan, W. M., & Katsaros, K. B. (1997). The air-sea momentum flux in conditions of wind sea and swell. *Journal of Physical Oceanography*, *27*(10), 2087–2099. https://doi.org/10.1175/1520-0485(1997)027<2087:tasmfi>2.0.co;2

Field, P. R., & Wood, R. (2007). Precipitation and cloud structure in midlatitude cyclones. *Journal of Climate*, *20*(2), 233–254. https://doi.org/10.1175/JCLI3998.1

Gonzalez, R. C., Woods, R. E., & Eddins, S. L. (2020). *Digital image processing using MATLAB* (3rd ed.). Gatesmark Publishing.

Gramcianinov, C. B., Campos, R. M., de Camargo, R., Hodges, K. I., Guedes Soares, C., & da Silva Dias, P. L. (2020). Analysis of Atlantic extratropical storm tracks characteristics in 41 years of ERA5 and CFSR/CFSv2 databases. *Ocean Engineering*, *216*, 108111. https://doi.org/10.1016/j.oceaneng.2020.108111

Gramcianinov, C. B., Hodges, K. I., & Camargo, R. (2019). The properties and genesis environments of South Atlantic cyclones. *Climate Dynamics*, *53*(7–8), 4115–4140. https://doi.org/10.1007/s00382-019-04778-1

Greeves, C. Z., Pope, V. D., Stratton, R. A., & Martin, G. M. (2007). Representation of Northern Hemisphere winter storm tracks in climate models. *Climate Dynamics*, *28*(7–8), 683–702. https://doi.org/10.1007/s00382-006-0205-x

Hanafin, J. A., Quilfen, Y., Ardhuin, F., Sienkiewicz, J., Queffeulou, P., Obrebski, M., et al. (2012). Phenomenal sea states and swell from a North Atlantic storm in February 2011: A comprehensive analysis. *Bulletin of the American Meteorological Society*, *93*(12), 1825–1832. https://doi.org/10.1175/BAMS-D-11-00128.1

Hart, R. E., & Evans, J. L. (2001). A climatology of the extratropical transition of Atlantic tropical cyclones. *Journal of Climate*, *14*(4), 546–564. https://doi.org/10.1175/1520-0442(2001)014<0546:acotet>2.0.co;2

Hersbach, H., Bell, B., Berrisford, P., Hirahara, S., Horányi, A., Muñoz-Sabater, J., et al. (2020). The ERA5 global reanalysis. *Quarterly Journal of the Royal Meteorological Society*, *146*(730), 1999–2049. https://doi.org/10.1002/qj.3803

Hewson, T. D., & Neu, U. (2015). Cyclones, windstorms and the IMILAST project. *Tellus, Series A: Dynamic Meteorology and Oceanography*, *6*(1), 27128. https://doi.org/10.3402/tellusa.v67.27128

Hodges, K. I., Hoskins, B. J., Boyle, J., & Thorncroft, C. (2003). A comparison of recent reanalysis datasets using objective feature tracking: Storm tracks and tropical easterly waves. *Monthly Weather Review*, *131*(9), 2012–2037. https://doi.org/10.1175/1520-0493(2003)131<2012:acorrd>2.0.co;2

Holliday, N. P., Yelland, M. J., Pascal, R., Swail, V. R., Taylor, P. K., Griffiths, C. R., & Kent, E. (2006). Were extreme waves in the Rockall Trough the largest ever recorded? *Geophysical Research Letters*, *33*(5), 2–5. https://doi.org/10.1029/2005GL025238

Holthuijsen, L. H., Powell, M. D., & Pietrzak, J. D. (2012). Wind and waves in extreme hurricanes. *Journal of Geophysical Research*, *117*(9). https://doi.org/10.1029/2012JC007983

Hoskins, B. J., & Hodges, K. I. (2002). New perspectives on the Northern Hemisphere winter storm tracks. *Journal of the Atmospheric Sciences*, *59*(6), 1041–1061. https://doi.org/10.1175/1520-0469(2002)059<1041:npotnh>2.0.co;2

Hoskins, B. J., & Hodges, K. I. (2005). A new perspective on Southern Hemisphere storm tracks. *Journal of Climate*, *18*(20), 4108–4129. https://doi.org/10.1175/JCLI3570.1

Izaguirre, C., Méndez, F. J., Menéndez, M., & Losada, I. J. (2011). Global extreme wave height variability based on satellite data. *Geophysical Research Letters*, *38*(10). https://doi.org/10.1029/2011GL047302

Jones, S. C., Harr, P. A., Abraham, J., Bosart, L. F., Bowyer, P. J., Evans, J. L., et al. (2003). The extratropical transition of tropical cyclones: Forecast challenges, current understanding, and future directions. *Weather and Forecasting*, *18*(6), 1052–1092. https://doi.org/10.1175/1520-0434(2003)018<1052:tetotc>2.0.co;2

Kita, Y., Waseda, T., & Webb, A. (2018). Development of waves under explosive cyclones in the Northwestern Pacific. *Ocean Dynamics*, *68*(10), 1403–1418. https://doi.org/10.1007/s10236-018-1195-z

Machado, J. P., Justino, F., & Souza, C. D. (2021). Influence of El Niño-Southern Oscillation on baroclinic instability and storm tracks in the Southern Hemisphere. *International Journal of Climatology*, *41*(S1), E93–E109. https://doi.org/10.1002/joc.6651

Mailier, P. J., Stephenson, D. B., Ferro, C. A., & Hodges, K. I. (2006). Serial clustering of extratropical cyclones. *Monthly Weather Review*, *134*(8), 2224–2240. https://doi.org/10.1175/MWR3160.1

Marshall, J., Kushnir, Y., Battisti, D., Chang, P., Czaja, A., Dickson, R., et al. (2001). North Atlantic climate variability: Phenomena, impacts and mechanisms. *International Journal of Climatology*, *21*(15), 1863–1898. https://doi.org/10.1002/joc.693

Murray, R. J., & Simmonds, I. (1991). A numerical scheme for tracking cyclone centres from digital data Part I: Development and operation of the scheme. *Australian Meteorological Magazine*, *39*(3), 155–166.

NASA Earth Observations. (2022). TRUE COLOR (1 DAY - NPP/VIIRS) [Dataset]. Retrieved from https://neo.gsfc.nasa.gov/view.php?datasetId=VIIRS_543D

Nelson, J., & He, R. (2012). Effect of the Gulf Stream on winter extratropical cyclone outbreaks. *Atmospheric Science Letters*, *13*(4), 311–316. https://doi.org/10.1002/asl.400

Neu, U., Akperov, M. G., Bellenbaum, N., Benestad, R., Blender, R., Caballero, R., et al. (2013). IMILAST: A community effort to intercompare extratropical cyclone detection and tracking algorithms. *Bulletin of the American Meteorological Society*, *94*(4), 529–547. https://doi.org/10.1175/BAMS-D-11-00154.1

NOAA/National Weather Service. (2022). North Atlantic Oscillation Index [Dataset]. National Centers for Environmental Prediction Climate Prediction Center. Retrieved from https://www.cpc.ncep.noaa.gov/products/precip/CWlink/pna/nao.shtml

Pinto, J. G., Spangehl, T., Ulbrich, U., & Speth, P. (2005). Sensitivities of a cyclone detection and tracking algorithm: Individual tracks and climatology. *Meteorologische Zeitschrift*, *14*(6), 823–838. https://doi.org/10.1127/0941-2948/2005/0068

Pinto, J. G., Zacharias, S., Fink, A. H., Leckebusch, G. C., & Ulbrich, U. (2009). Factors contributing to the development of extreme North Atlantic cyclones and their relationship with the NAO. *Climate Dynamics*, *32*(5), 711–737. https://doi.org/10.1007/s00382-008-0396-4

Ponce de León, S., & Bettencourt, J. H. (2021). Composite analysis of North Atlantic extra-tropical cyclone waves from satellite altimetry observations. *Advances in Space Research*, *68*(2), 762–772. https://doi.org/10.1016/j.asr.2019.07.021

Ponce de León, S., & Guedes Soares, C. (2014). Extreme wave parameters under North Atlantic extratropical cyclones. *Ocean Modelling*, *81*, 78–88. https://doi.org/10.1016/j.ocemod.2014.07.005

Queffeulou, P. (2004). Long-term validation of wave height measurements from altimeters. *Marine Geodesy*, *27*(3–4), 495–510. https://doi.org/10.1080/01490410490883478

Ribal, A., & Young, I. R. (2019). 33 years of globally calibrated wave height and wind speed data based on altimeter observations. *Scientific Data*, *6*(1), 77. https://doi.org/10.1038/s41597-019-0083-9

Rudeva, I., & Gulev, S. K. (2007). Climatology of cyclone size characteristics and their changes during the cyclone life cycle. *Monthly Weather Review*, *135*(7), 2568–2587. https://doi.org/10.1175/MWR3420.1

Rudeva, I., & Gulev, S. K. (2011). Composite analysis of North Atlantic extratropical cyclones in NCEP-NCAR reanalysis data. *Monthly Weather Review*, *139*(5), 1419–1446. https://doi.org/10.1175/2010MWR3294.1

Schneidereit, A., Blender, R., & Fraedrich, K. (2010). A radius-depth model for midlatitude cyclones in reanalysis data and simulations. *Quarterly Journal of the Royal Meteorological Society*, *136*(646), 50–60. https://doi.org/10.1002/qj.523

Serreze, M. (2009). Northern Hemisphere cyclone locations and characteristics from NCEP/NCAR reanalysis data, version 1.

Serreze, M. C., Carse, F., Barry, R. G., & Rogers, J. C. (1997). Icelandic low cyclone activity: Climatological features, linkages with the NAO, and relationships with recent changes in the Northern Hemisphere circulation. *Journal of Climate*, *10*(3), 453–464. https://doi.org/10.1175/1520-0442(1997)010<0453:ilcacf>2.0.co;2

Sinclair, M. R. (1994). An objective cyclone climatology for the Southern Hemisphere. *Monthly Weather Review*, *122*(10), 2239–2256. https://doi.org/10.1175/1520-0493(1994)122<2239:aoccft>2.0.co;2

Takbash, A., Young, I. R., & Breivik, Ø. (2019). Global wind speed and wave height extremes derived from long-duration satellite records. *Journal of Climate*, *32*(1), 109–126. https://doi.org/10.1175/JCLI-D-18-0520.1

Timmermans, B. W., Gommenginger, C. P., Dodet, G., & Bidlot, J. R. (2020). Global wave height trends and variability from new multimission satellite altimeter products, reanalyses, and wave buoys. *Geophysical Research Letters*, *47*(9), 1–11. https://doi.org/10.1029/2019GL086880

Trigo, I. F., Davies, T. D., & Bigg, G. R. (1999). Objective climatology of cyclones in the Mediterranean region. *Journal of Climate*, *12*(6), 1685–1696. https://doi.org/10.1175/1520-0442(1999)012<1685:ococit>2.0.co;2

Ulbrich, U., Leckebusch, G. C., & Pinto, J. G. (2009). Extra-tropical cyclones in the present and future climate: A review. In *Theoretical and applied climatology* (Vol. 96, pp. 117–131). Springer Wien. https://doi.org/10.1007/s00704-008-0083-8

Vincent, L. (1993). Morphological grayscale reconstruction in image analysis: Applications and efficient algorithms. *IEEE Transactions on Image Processing*, *2*(2), 176–201. https://doi.org/10.1109/83.217222

Wallace, J. M., & Hobbs, P. V. (2006). *Atmospheric science: An introductory survey* (Vol. 9, 2nd ed.). Elsevier Inc.

Wang, X. L., Swail, V. R., & Zwiers, F. W. (2006). Climatology and changes of extratropical cyclone activity: Comparison of ERA-40 with NCEP-NCAR reanalysis for 1958–2001. *Journal of Climate*, *19*(13), 3145–3166. https://doi.org/10.1175/JCLI3781.1

Wang, X. L., Wan, H., & Swail, V. R. (2006). Observed changes in cyclone activity in Canada and their relationships to major circulation regimes. *Journal of Climate*, *19*(6), 896–915. https://doi.org/10.1175/JCLI3664.1

Wright, C. W., Walsh, E. J., Vandemark, D., Krabill, W. B., Garcia, A. W., Houston, S. H., et al. (2001). Hurricane directional wave spectrum spatial variation in the open ocean. *Journal of Physical Oceanography*, *31*(8), 2472–2488. https://doi.org/10.1175/1520-0485(2001)031<2472:hdwssv>2.0.co;2

Xie, N., Sun, Y., & Gao, M. (2020). The influence of five teleconnection patterns on wintertime extratropical cyclones over northwest Pacific. *Atmosphere*, *11*(11), 1–17. https://doi.org/10.3390/atmos11111248

Young, I. R., & Donelan, M. A. (2018). On the determination of global ocean wind and wave climate from satellite observations. *Remote Sensing of Environment*, *215*, 228–241. https://doi.org/10.1016/j.rse.2018.06.006

Young, I. R., Fontaine, E., Liu, Q., & Babanin, A. V. (2020). The wave climate of the Southern Ocean. *Journal of Physical Oceanography*, *50*(5), 1417–1433. https://doi.org/10.1175/JPO-D-20-0031.1

Young, I. R., & Vinoth, J. (2013). An "extended fetch" model for the spatial distribution of tropical cyclone wind-waves as observed by altimeter. *Ocean Engineering*, *70*, 14–24. https://doi.org/10.1016/j.oceaneng.2013.05.015

Zieger, S., Vinoth, J., & Young, I. R. (2009). Joint calibration of multiplatform altimeter measurements of wind speed and wave height over the past 20 years. *Journal of Atmospheric and Oceanic Technology*, *26*(12), 2549–2564. https://doi.org/10.1175/2009JTECHA1303.1